Mechanical Performance of Circular Ultrahigh-Performance Concrete–Filled Double Skin High-Strength Steel Tubular Stub Columns under Axial Compression

Bo Yang[1]; Le Shen[2]; Kang Chen[3]; Chen Feng[4]; Xuchuan Lin[5]; Mohamed Elchalakani[6]; and Shaoqian Xu[7]

Abstract: This paper proposed a new type of stiffened circular ultra-high performance concrete-filled double skin steel tubular (UHPCFDST) column, in which stiffeners were applied to connect both inner and outer steel tubes. It efficiently delayed the local buckling of steel tubes and enhanced the integral of the section. This new type of UHPCFDST can be named multicells ultra-high performance concrete-filled double skin steel tubular (MUHPCFDST) column since the stiffener divided the sandwich space between the two steel tubes into multicells. Both the UHPCFDST and MUHPCFDST stub columns were fabricated and tested under centrally compression loading to investigate the axial mechanical behavior. The parameters considered in this study included specimen size, diameter-to-thickness ratio, the quantity of stiffener, and hollow ratio. Based on the tests, specimens' column failure mode, axial load-shortening curves, local buckling behavior, compounding strength, strength index, and ductility coefficient were obtained and discussed. Then, the authors proposed a uniaxial stress-strain function of ultra-high performance concrete under compression and established three-dimension finite-element (FE) models with this stress-strain model to simulate the axial behavior of UHPCFDST and MUHPCFDST columns. Compared with the experimental results, the average deviation of the FE analysis in predicting the column bearing capacity and corresponding axial shortening was -3% and -5.5%, respectively. Finally, parametric studies were carried out, and a calculation method was proposed. The parametric analysis results and predictions from different methods (including the proposed method and methods suggested by existing design codes) were compared. The proposed method and calculating methods provided in AIJ-2008, EC4, and AS/NZS 2327 can reasonably predict the ultimate bearing capacity of both circular UHPCFDST and circular MUHPCFDST columns. **DOI: 10.1061/(ASCE)ST.1943-541X.0003291.** © *2021 American Society of Civil Engineers.*

Author keywords: Ultra-high performance concrete; High-strength steel; Concrete-filled double skin steel tubular (CFDST); Stiffened CFDST; Finite-element (FE) analysis; Calculation method.

[1]Funding Agency, Key Laboratory of Earthquake Engineering and Engineering Vibration, Institute of Engineering Mechanics, China Earthquake Administration, 63 Fuxing Rd., Beijing 100036, China; Professor, School of Civil Engineering, Chongqing Univ., 83 Shabeijie, Chongqing 400045, China. ORCID: https://orcid.org/0000-0001-5374-9208. Email: yang0206@cqu.edu.cn

[2]Ph.D. Candidate, School of Civil Engineering, Chongqing Univ., 83 Shabeijie, Chongqing 400045, China (corresponding author). Email: ryun2010@163.com

[3]Hongshen Lecturer, School of Civil Engineering, Chongqing Univ., 83 Shabeijie, Chongqing 400045, China. ORCID: https://orcid.org/0000-0002-5811-2043. Email: chen0429@cqu.edu.cn

[4]Postgraduate Student, School of Civil Engineering, Chongqing Univ., 83 Shabeijie, Chongqing 400045, China. Email: feng02210702@163.com

[5]Research Fellow, Key Laboratory of Earthquake Engineering and Engineering Vibration, Institute of Engineering Mechanics, China Earthquake Administration, 63 Fuxing Rd., Beijing 100036, China. Email: linxuchuan@iem.ac.cn

[6]Senior Lecturer, School of Civil, Environmental, and Mining Engineering, Univ. of Western Australia, Crawley, WA 6009, Australia. Email: mohamed.elchalakani@uwa.edu.au

[7]Lecturer, School of Civil Engineering, Chongqing Univ., 83 Shabeijie, Chongqing 400045, China. Email: xsq1963@163.com

Introduction

Concrete-filled double skin steel tubular (CFDST) is a new type of hollow-core steel-concrete composite structure and develops from a concrete-filled steel tubular (CFST) structure. It consists of an outer steel tube and an inner steel tube, and concrete is used to fill the space between the two tubes (Wei et al. 1995; Zhao et al. 2002; Tao and Han 2006; Liang 2017, 2018). Therefore, the CFDST column inherits the CFST column's merits, including high-strength, good ductility performance, high fire resistance (Lu et al. 2010a, b), and favorable constructability. Furthermore, attributed to the unique sectional configuration, the CFDST structure has been proved to possess higher bending stiffness-weight ratio (Han et al. 2019) and better cyclic performance (Han et al. 2006) than the CFST structure. Nowadays, CFDST is widely used in high-rise buildings (Ayough et al. 2020), electrical grid infrastructures, wind turbine towers, and bridge piers.

Due to these merits, researchers developed various new types of CFDST members using new materials, such as high and ultra-high-strength steel (Fang and Lin 2014; Hsiao et al. 2015; Farahi et al. 2017; Xiong et al. 2017a; Teng et al. 2018; Li and Cai 2019), stainless steel (Han et al. 2009; Uy et al. 2011; Li et al. 2018), rubberized concrete (Duarte et al. 2016; Elchalakani et al. 2018; Khusru et al. 2020), high-strength concrete (Ahmed et al. 2019a, b; Ekmekyapar et al. 2019), and ultra-high performance concrete
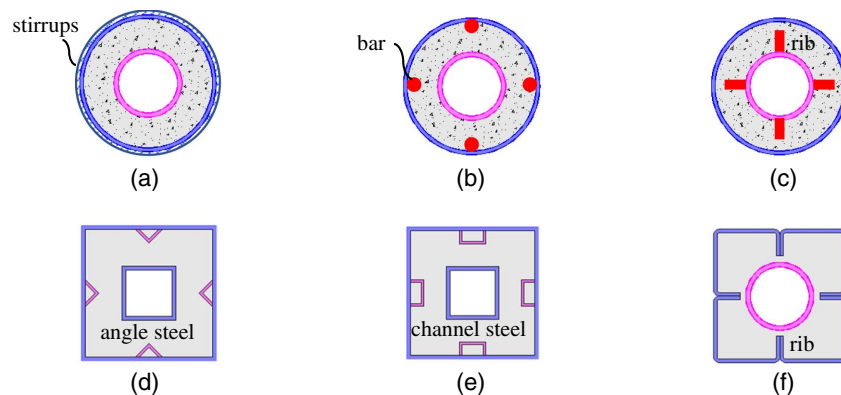
Fig. 1. Stiffened CFDST structures: (a) stiffened by annular stirrups; (b) stiffened by bars; (c) stiffened by ribs; (d) stiffened by angle steels; (e) stiffened by U-steels; and (f) thin-walled steel tube.

(UHPC) (Wang et al. 2019; Xiong 2012; Zhang et al. 2015; Yan et al. 2021). As a well-known cement material, UHPC has excellent mechanical properties (Richard and Cheyrezy 1995; Habel et al. 2006; Graybeal 2007; Kang et al. 2010; Krahl et al. 2019) (especially the high compressive strength) and durability (Zhou and Qiao 2018; Chu et al. 2020) compared with normal-strength concrete or high-strength concrete. Therefore, under the same loading conditions, the use of UHPC will considerably decrease the dimension of structural members, reduce the usage of concrete, and increase the available space of the structure. Previous research studies (Xiong et al. 2017a, b; Chen et al. 2018; Yan et al. 2019; Cai et al. 2021a, b) have demonstrated the excellent mechanical properties of the UHPCFDST/UHPCFST members. In these studies, the small diameter-to-thickness ratio steel tube was used to ensure the composite effect of steel tube and concrete and avoid the occurrence of local bucking of steel tube before peak loads. However, it will lead to a high steel ratio, implying a high cost. To prevent or delay local buckling, various stiffened CFDST columns have been proposed by researchers (Dong and Ho 2013; Masaru et al. 2013; Hasan and Ekmekyapar 2019; Liang et al. 2019; Mohammadbagheri and Shekastehband 2020; Wang et al. 2020), as shown in Fig. 1. Corresponding experimental results show that these stiffeners can delay the local buckling effectively. However, these stiffeners were only applied to stiffen outer or inner steel tubes. To improve the utilization of stiffeners and enhance the integrity of the section, the authors proposed a new method in which strips were used to connect to the two steel tubes to stiffen the CFDST column (Ding et al. 2019; Alqawzai et al. 2020; Shen et al. 2022), as shown in Fig. 2. This new type of stiffened CFDST can be named multicells CFDST (MCFDST) since strips divide the sandwich space into multicaves. Experimental results showed that this new method could delay the local buckling of steel tubes efficiently and significantly improve the composite effect of concrete and steel tubes.
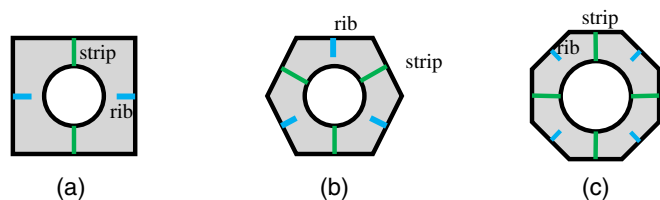
It can be predicted that using high-strength steel and UHPC in the MCFDST can efficiently reduce the usage of concrete and steel, and the whole member can be called multicells ultra-high performance concrete-filled double skin steel tubular (MUHPCFDST).
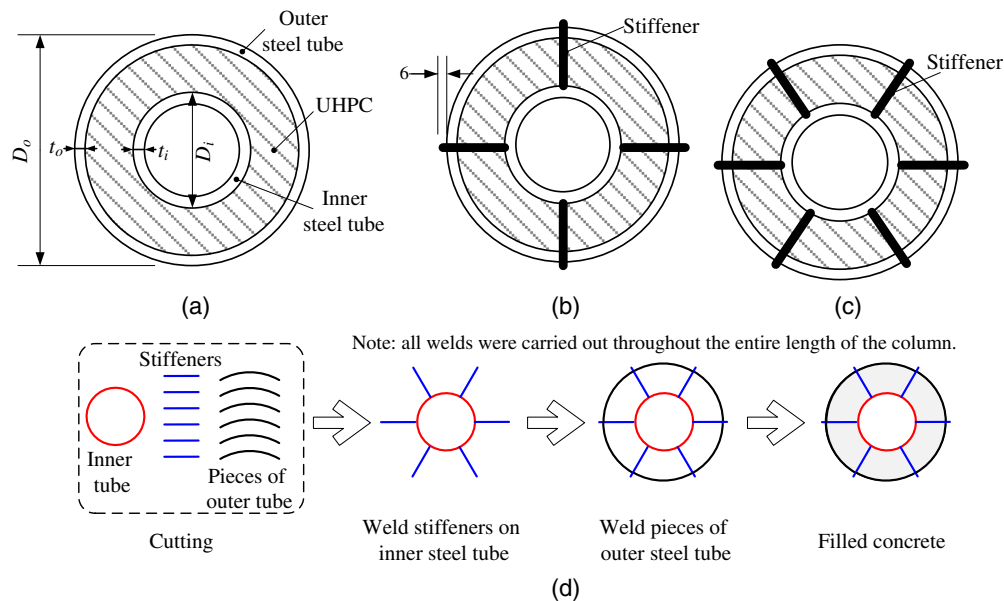
However, as a new type of composite column, few studies were carried on the mechanical behavior of MUHPCFDST columns. The current studies on the mechanical behavior of the MCFDST members focused on the square (Ding et al. 2019), hexagonal (Shen et al. 2022), and octagon sections with common strength materials (Alqawzai et al. 2020). For the member with high-strength steel and UHPC, the interaction mechanism between steel tube and concrete is still not clarified, let alone the circular members. Undoubtedly, it will become an obstacle to the engineering application of the MUHPCFDST structure. Therefore, further studies are necessary to reveal the mechanical behavior of the MUHPCFDST members.

In this study, nine short columns with ultra-high-performance concrete and high-strength steel were fabricated and tested considering the parameters of specimen size, steel tube thickness, quantity of stiffener, and hollow ratio. The failure modes, axial load-shortening curves, compounding strength, and ductility coefficient were obtained and analyzed in detail. Then, a new strain hardening/softening function of unconfined and confined UHPC was proposed for the finite-element (FE) model. Finally, predictions from different methods in existing design codes were compared and discussed based on the parametric study results.

Experimental Program

Specimen Design and Fabrication

A total of nine members were manufactured and tested, including five circular UHPCFDST columns and four circular MUHPCFDST columns. The stiffeners (4 mm) were extended to the outer steel tube by 6 mm to ensure the welding, as shown in Figs. 3(a–c), and the fabricated process of the MUHPCFDST column is illustrated in Fig. 3(d). A length-to-width ratio (L/D_o) of 3 was chosen to reduce the end effects and ensure that the specimens would be stub columns with little impact from columns slenderness (Martin and Bridge 1997; Zhou et al. 2019; Alqawzai et al. 2020; Ding 2020). The previous studies pointed out that the strength between concrete and steel of the CFST column should be well matched to ensure a desirable composite effect (Ozbakkaloglu and Idris 2014; Zhang et al. 2019). High-strength steel (HG785D steel with yield strength higher than 690 MPa) was adopted in this study.

Fig. 2. The new type of stiffened CFDST: (a) stiffened square section; (b) stiffened hexagonal section; and (c) stiffened octagon section.

Fig. 3. Cross sections of test members and fabricated specimen process: (a) UHPCFDST; (b) MUHPCFDST with four stiffeners; (c) MUHPCFDST with six stiffeners; and (d) fabricated process of MUHPCFDST column. Note: All welds were carried out throughout the entire length of the column.

Table 1. Details of specimens

Specimen	L (mm)	D_o mm	t_o mm	D_i mm	t_i (mm)	n_s (mm)	f_{yo} (MPa)	f_{yi} (MPa)	f_c (MPa)	γ_u	ξ	ψ	χ
C203-4-76	600	203	4	76	4	—	711.2	450.0	97.1	0.925	0.663	50.75	0.390
C203-4-114	600	203	4	114	4	—	711.2	378.0	106.9	0.925	0.602	50.75	0.585
C203-6-114	600	203	6	114	4	—	770.5	378.0	106.7	0.927	1.009	33.83	0.597
C300-6-203A	900	300	6	203	4	—	770.5	711.2	106.7	0.886	0.693	50	0.705
C300-6-203B	900	300	6	203	4	—	770.5	711.2	97.1	0.886	0.762	50	0.705
MC203-4-76	600	203	4	76	4	4	711.2	450.0	110.8	0.925	0.581	50.75	0.390
MC203-4-114	600	203	4	114	4	4	711.2	378.0	108.9	0.925	0.591	50.75	0.585
MC203-6-114	600	203	6	114	4	6	770.5	378.0	106.2	0.927	1.013	33.83	0.597
MC300-6-203	900	300	6	203	4	6	770.5	711.2	106.2	0.886	0.696	50	0.705

Note: ξ = the nominal confinement factors (Tao and Han 2006); $\chi = D_i/(D_o - 2t_o)$ = hollow ratio; ψ = diameter-to-thickness ratio of outer steel tube; and n_s = quantity of stiffener.

The column details are summarized in Table 1, where ξ and χ are the nominal confinement factors and hollow ratio (Tao and Han 2006), respectively. The value of ξ and χ can be calculated by Eqs. (1)–(4)

$$\xi = \frac{A_{so}f_{yo}}{A_{ce}f_{c,e}} \quad (1)$$

$$f_{c,e} = \gamma_u f_c \quad (2)$$

$$A_{ce} = 0.25\pi(D_o - 2t_o)^2 \quad (3)$$

$$\chi = \frac{D_i}{D_o - 2t_o} \quad (4)$$

where A_{so} and A_{ce} = area of the outer steel tube and the nominal cross-sectional area of concrete (Han et al. 2019), respectively; and γ_u = strength reduction factor for concrete considering the size effect (Sakino et al. 2004).

In addition, the UHPCFDST and MUHPCFDST specimens were named as $Cxxx - t_o - D_i$ and $MCxxx - t_o - D_i$, respectively. Where xxx, t_o, and D_i are the outer tube diameter D_o, outer tube thickness t_o, and inner tube diameter D_i of the specimen,

respectively, as shown in Fig. 3. For instance, C203-4-76 represents a circular UHPCFDST column, the outer tube size is $\phi203 \times 4$, and the inner tube diameter is 76 mm. By contrast, MC203-4-76 represents a circular MUHPCFDST column with the same dimensions as Specimen C203-4-76.

The fabricating process of a typical MUHPCFDST member is illustrated in Fig. 3(d). First, a long seamless steel tube was cut into small pieces, namely components. Alternatively, a Grade HG785D steel plate can also be used to fabricate the outer tube components. The pieces would then be bent into an arc shape. Stiffeners were also cut from steel plates with the required strength. The second step was to weld all of the stiffeners on the inner steel tube. After that, the arc-shaped pieces were welded and formed the outer steel tube. Finally, UHPC was cast into the welded steel component. It is worth noting that all the welds were carried out throughout the entire length of the column.

Material Properties

UHPC-120 was adopted during the fabrication of the test specimens. The UHPC was prepared with binder materials (B, including cement and silica fume), water (W), polycarboxylate Superplasticizer (SP), quartz sand (QS), and straight type steel fibers (SFs)

Table 2. The mix proportion of UHPC-120 (kg/m³)

Grade	B	QS	SP	SF	W
UHPC-120	1,159	924	22.9	158	195.8

with a fixed length of 13 mm and a fixed diameter of 0.2 mm. The mix proportion of UHPC-120 is shown in Table 2. According to ASTM C39/C39M-05 (ASTM 1999), three cylindrical specimens with a dimension of $\phi100$ mm $\times$ 200 mm were prepared and tested to obtain the axial compressive strength (28 days). The test results are summarized in Table 1.

The high-strength steel of HG785D [produced by Wuhan Iron and Steel (Group) Company] was adopted to fabricate the steel tubes and stiffeners. The Q345 seamless circular steel tube was adopted for the steel tube with a small diameter (less than 180 mm) since it is hard to fabricate small diameter round tubes with the high-strength steel plate. Four groups of dog-bone shape tensile specimens were prepared and tested based on GB/T 228.1-2010 (MOHURD 2010b). The test results are summarized in Table 3, where f_y is the yield strength, f_u is the ultimate tensile strength, E_s is the elastic modulus, ε_p is the yield strain, and ε_y is the strain at the end of the yield plateau. In addition, the stress-strain curves of the samples are presented in Fig. 4.

Test Setup and Instrumentation

Chongqing university's 20 MN capacity testing machine was used for the axial compression tests, as shown in Fig. 5(a). In the study, four LVDTs were used to measure the axial shortening. In addition, three inclinator inclinometers and six 1080p cameras were used to monitor the machine's rotation and record the test, respectively. Axial loads were applied at a rate of 3 kN/s at the elastic stage,

whereas displacement control at a rate of 0.5 mm/min was activated after the slope of the axial load-shortening curve changed. Testing ended when the load decreased to about 30% of the ultimate load or the axial displacement reached 0.05L. Locations of strain gages are shown in Fig. 5(b). Previous studies have shown that due to the existence of end buckling modes, strengthening the end may improve the bearing capacity of the specimen, resulting in an unconservative design (Alqawzai et al. 2020). Therefore, the load was directly applied to the column top without stiffener at the column ends in this work. Before the test, the specimen was carefully placed by using a laser to make it vertically aligned.

Experimental Results and Discussion

This section presents and discusses the test specimens' failure mode, axial loading-shortening curve, local buckling, compound axial strength, strength index, and ductility performance. The ultimate bearing capacity (N_u) of the test specimens is summarized in Table 4.

Failure Modes

Fig. 6 presents the typical failure modes of the UHPCFDST specimens. Visible local buckling (or bulges) generated on both the outer and inner steel tubes and evident oblique cracking appeared on the sandwich UHPC. Moreover, for most UHPCFDST specimens, visible cracks also occurred at the weld, except for Specimen C203-4-114. In addition, for Specimens C203-4-76 and C203-4-114, there were significant scratches on the sandwich concrete caused by the sliding between the concrete and the outer steel tube. As for the MUHPCFDST specimens, local buckling (or bulges) and steel tube cracks also appeared, as shown in Fig. 7. However, compared with UHPCFDST columns, the sandwich UHPC of the MUHPCFDST

Table 3. Material properties of steel tubes

Materials	Thickness (mm)	E_s (GPa)	f_y (MPa)	f_u (MPa)	ε_p ($\mu\varepsilon$)	ε_y ($\mu\varepsilon$)
HG785D	4	220.2	711.2	774.6	3,230	22,161
	6	227.6	770.5	825.0	3,385	16,211
Seamless steel tube	$\phi76 \times 4$	206.0	450.0	596.9	2,184	22,967
	$\phi114 \times 4$	206.0	378.0	537.8	1,835	20,268
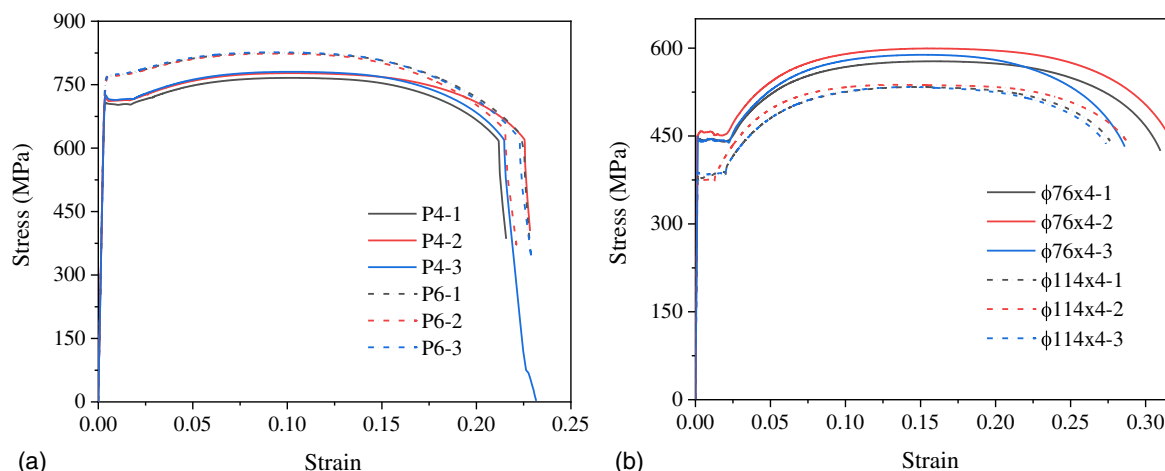
Fig. 4. Full stress-strain curves up to the failure of tensile tests: (a) steel plate; and (b) seamless steel tube.
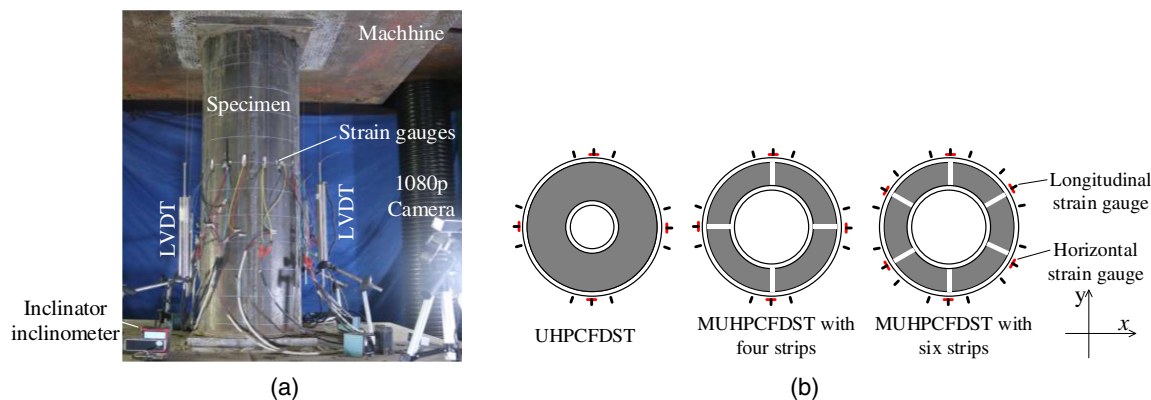
Fig. 5. Test setup and instrumentation: (a) test setup; and (b) location of strain gauges.

Table 4. Summary of the test results

specimen	ξ	χ	α	Δ_b mm	N_b kN	Δ_u mm	N_u (kN)	f_{osc} MPa	SI	Δ_b/Δ_u
C203-4-76	0.663	0.390	0.099	5.151	5,478.7	4.779	5,572.1	184.0	1.237	1.078
C203-4-114	0.602	0.585	0.127	3.904	4,719.3	4.018	4,751.4	189.1	1.109	0.972
C203-6-114	1.009	0.597	0.201	4.345	5,944.5	4.282	6,081.5	249.2	1.160	1.015
C300-6-203A	0.693	0.705	0.169	3.400	9,594.0	4.048	9,783.8	207.1	1.062	0.840
C300-6-203B	0.762	0.705	0.169	4.106	9,386.0	4.487	9,438.3	198.0	1.056	0.915
MC203-4-76	0.581	0.390	0.099	8.638	6,255.6	5.017	6,739.4	200.3	1.229	1.722
MC203-4-114	0.591	0.585	0.127	4.399	5,805.8	4.020	6,158.4	229.9	1.292	1.094
MC203-6-114	1.013	0.597	0.201	12.866	6,675.0	4.989	7,122.0	263.5	1.258	2.579
MC300-6-203	0.696	0.705	0.169	7.869	11,127.7	7.649	11,154.9	222.2	1.153	1.029

Note: $\alpha = A_{so}/A_c$ = steel ratio, where A_c is the area of concrete; and Δ_b = axial shortening when local buckling occurred, while Δ_u = axial shortening corresponding to the peak loads; N_u = ultimate bearing capacity; f_{osc} = compound axial strength for the outer tube and the UHPC; and SI = strength index.
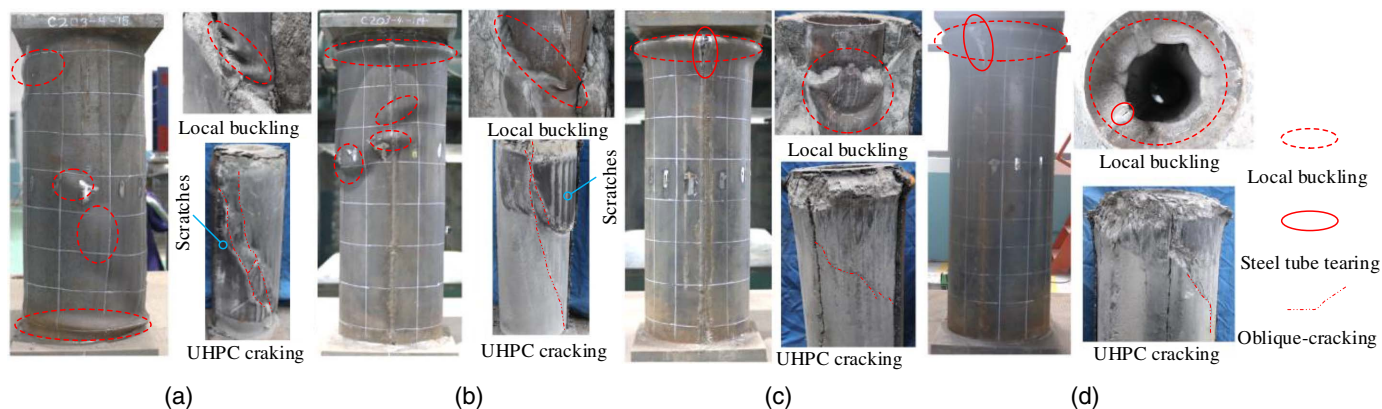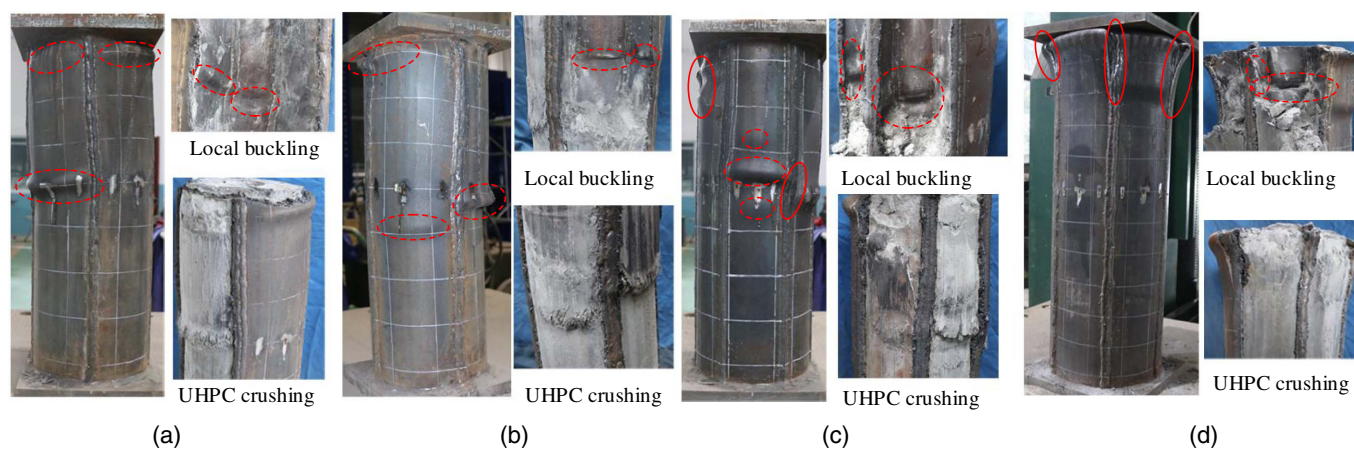

Fig. 6. Photos of the circular UHPCFDST specimens after testing: (a) C203-4-76; (b) C203-4-114; (c) C203-6-114; and (d) C300-6-203A.

specimens showed concrete crushing at the location of the bulges rather than oblique cracking. One possible reason is that the stiffeners divided the sandwich concrete into independent multicells, restricting the occurrence and development of the oblique cracking.
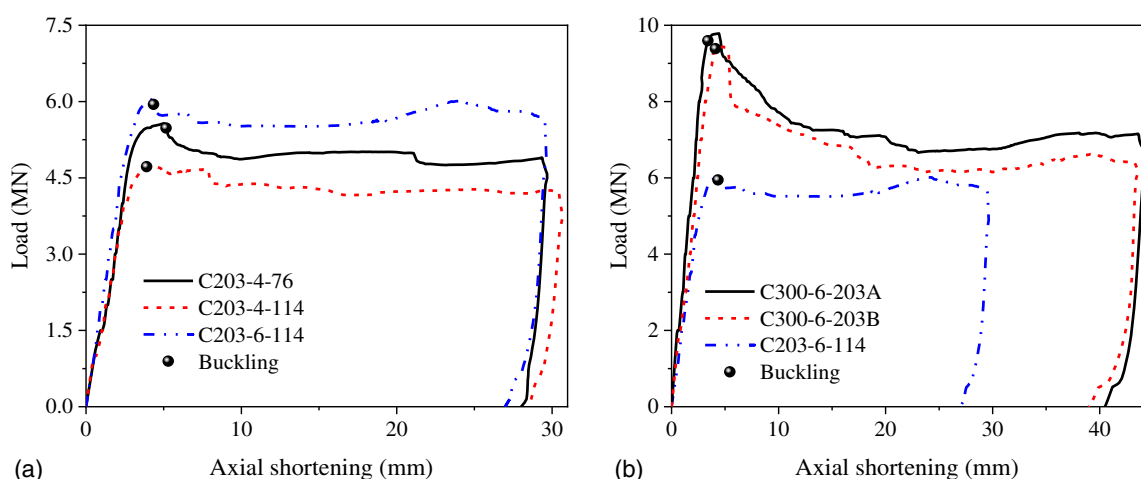
Axial Load-Shortening Behavior

The axial load-shortening curves of the circular UHPCFDST specimens are presented in Fig. 8. Generally, the axial load-shortening curve can be divided into three branches: (1) an approximately bilinear ascending branch; (2) descending branch caused by buckling of steel tube; and (3) an approximately stabilized branch, including

a slightly ascending branch. It can be found that the axial load-shortening curves of Specimens C203-4-76, C203-4-114, and C203-6-114 were significantly different from that of Specimens C300-6-203A and C300-6-203B, especially the descending branch. The diameter-to-thickness ratio of the inner tube for Specimens C203-4-76, C203-4-114, and C203-6-114 was much less than that of the outer tube (the limit diameter-to-thickness ratio of seamless steel was much greater than the steel tube fabricated by high-strength steels), as shown in Fig. 9. Thus, the inner tube would still keep working even though the buckling appeared on the outer tube, leading to a gradual descending branch. On the other hand, in Specimens C300-6-203A and C300-6-203B, the diameter-to-thickness

Fig. 7. Photos of the circular MUHPCFDST specimens after testing: (a) MC203-4-76; (b) MC203-4-114; (c) MC203-6-114; and (d) MC300-6-203.

Fig. 8. Load-axial shortening curves of circular UHPCFDST specimens: (a) $D_o = 203$ mm; and (b) $t_o = 6$ mm.
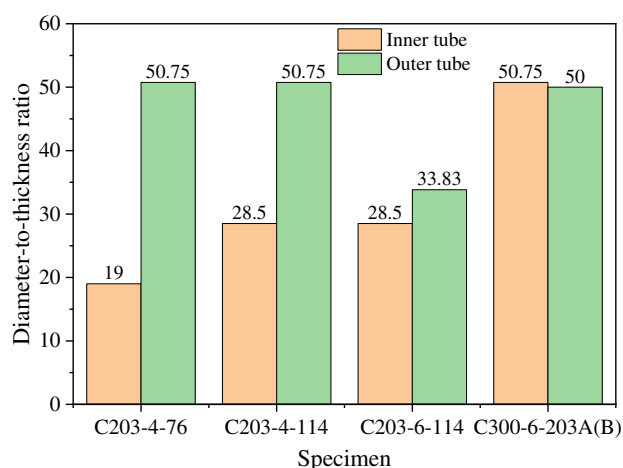

Fig. 9. Diameter-to-thickness ratio of circular UHPCFDST specimens.

ratio of the inner tube was very close to the outer one even though it did not exceed the limit value. In this condition, local buckling of the outer and inner steel tubes appeared simultaneously, accelerating the load drop, as shown in Fig. 8(b).

Similar to circular UHPCFDST specimens, the axial load-shortening curve of circular MUHPCFDST specimens can also be divided into three stages. At the same time, the load dropping phenomenon was significantly alleviated by the use of stiffeners, as shown in Fig. 10. More specifically, the local buckling of steel tubes was efficiently delayed because of stiffeners. However, a second descending branch of Specimen MC300-6-203 appeared when the axial shortening reached 22.2 mm (0.025L) due to weld cracking.

Load-Strain Curves

Fig. 11 shows the load-axial/hoop strain curves of the test specimens. In Fig. 11, the axial and hoop strains were the average of the data obtained from the longitude and hoop strain gages, respectively. For Specimen C203-6-114, C300-6-203A and MC300-6-203, because of the end failure mode, the axial/hoop strains negligibly change after the peak load, as shown in Figs. 11(c and d). For specimens with a sizable diameter-to-thickness ratio (greater or equal to 50), the load-strain curves of MUHPCFDST columns were much higher than that of the corresponding UHPCFDST columns, as shown in Figs. 11(a, b, and d). However, the load-strain curve of Specimen C203-6-114 was very close to that of Specimen MC203-6-114. It was attributed to the small diameter-to-thickness
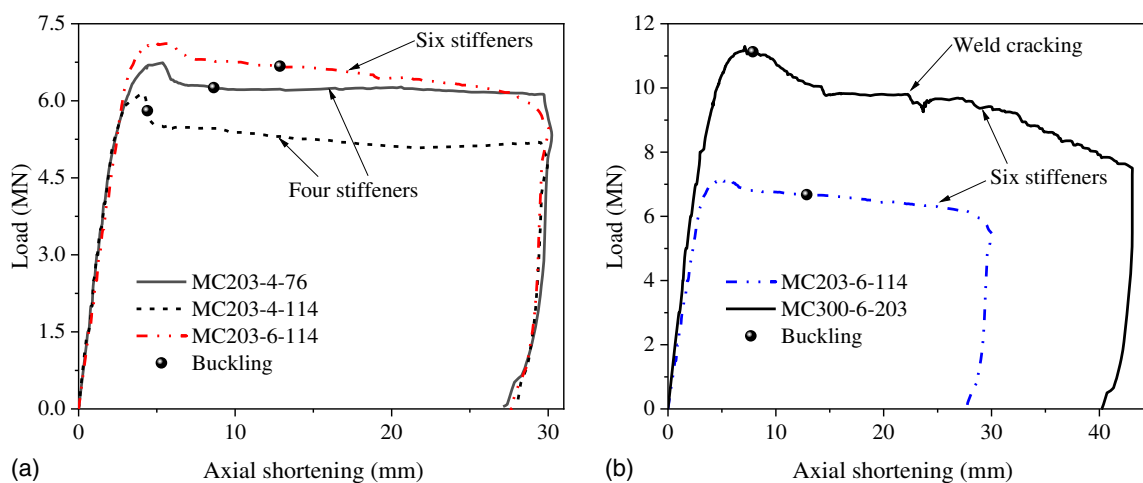
Fig. 10. Load-axial shortening curves of circular MUHPCFDST specimens: (a) $D_o = 203\ mm$; and (b) $t_o = 6\ mm$.
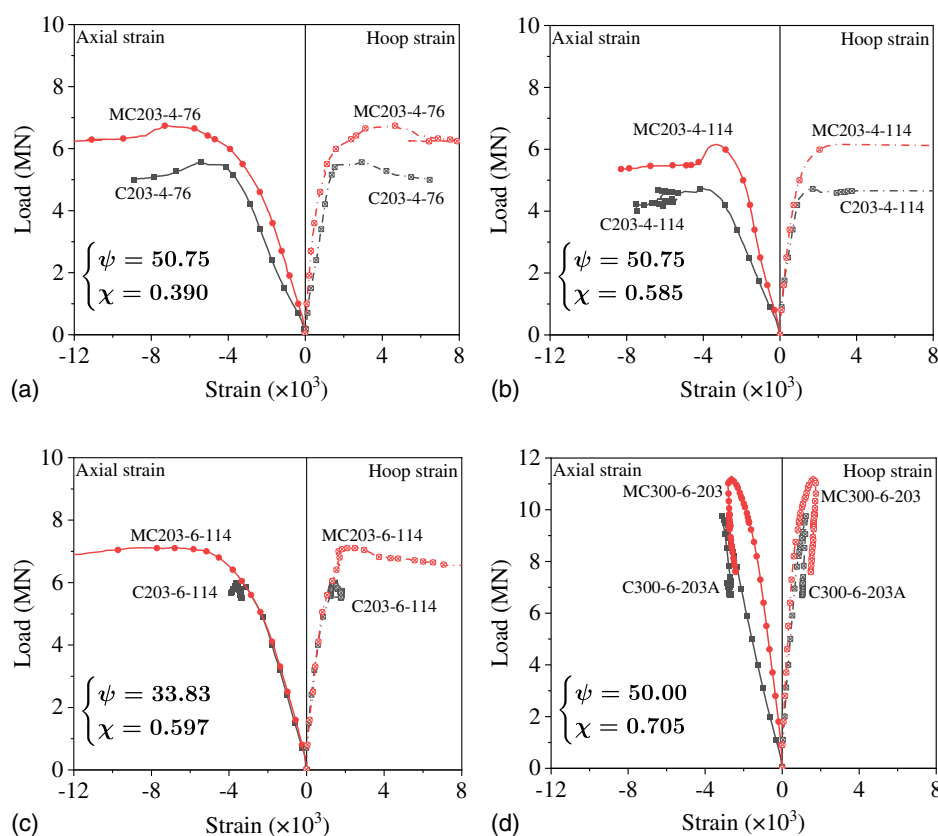
Fig. 11. Load-strain curves of test specimens: (a) C203-4-76 versus MC203-4-76; (b) C203-4-114 versus MC203-4-114; (c) C203-6-114 versus MC203-6-114; and (d) C300-6-203 versus MC300-6-203.

ratio of steel tubes. The steel tubes with a smaller diameter-to-thickness ratio were less prone to local buckling. However, it does not mean that the stiffeners were not helpful. On the contrary, it means that stiffeners can improve the composite effect between steel tubes and concrete for specimens with a small diameter-to-thickness ratio. Because the stiffeners increased the stiffness of the specimen circumferential deformation, the steel-concrete composite action of the MUHPCFDST specimen was stronger than that of the UHPCFDST specimen when the hoop strain was the same. It is also the reason why the load-strain curve of Specimen

MC203-6-114 still increased significantly after the strain exceeded the peak point strain of the Specimen C203-6-114, as shown in Fig. 11(c).

Local Buckling

Previous research studies showed that the behavior of CFST/CFDST columns was significantly affected by the buckling of steel tubes (Peng et al. 2018). To evaluate the buckling behavior, the ratio of Δ_b/Δ_u is defined, where Δ_b was the axial shortening when
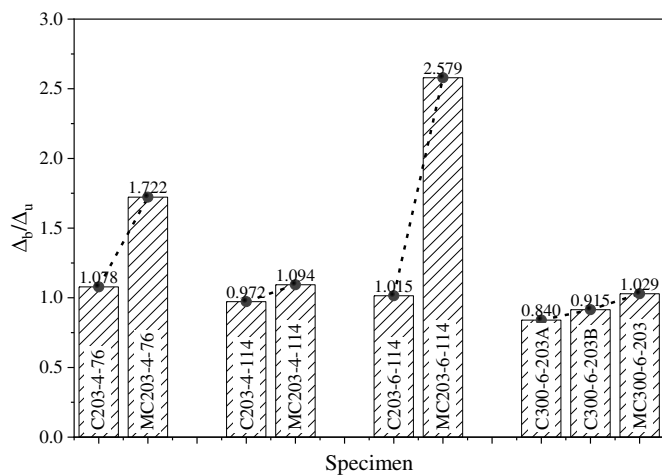
Fig. 12. The value of Δ_b/Δ_u of test specimens.

Fig. 13. Compound axial compressive strength of test columns.

buckling occurred, and Δ_u is the axial shortening corresponding to peak loads. The value of Δ_b/Δ_u is summarized in Fig. 12. When Δ_b/Δ_u is less than 1, meaning the local buckling occurs before the peak load. Otherwise, the local buckling occurs after the peak load. In other words, as the value of Δ_b/Δ_u increases, the occurrence of local buckling delays.

It can be seen that the value of Δ_b/Δ_u of the UHPCFDST specimen was much smaller than that of the MUHPCFDST specimen. For example, Δ_b/Δ_u of Specimen C203-4-76 was 1.078, which was considerably less than 1.772 of Specimen MC203-4-76. For all the MUHPCFDST specimens, the value of Δ_b/Δ_u was larger than unity, indicating that the stiffeners postponed the local buckling of the steel tube effectively. Furthermore, by comparing the value of Δ_b/Δ_u for Specimens C203-4-114 and C203-6-114 (or Specimens MC203-4-114 and MC203-6-114), it can be concluded that the local buckling could also be postponed by increasing the thickness of the steel tube.

Compound Axial Compressive Strength

The compound axial compressive strength (f_{osc}) was suggested by Han and Tao (2001) to predict the ultimate bearing capacity of concrete-filled steel tube columns. In this paper, the value of f_{osc} can be calculated by Eq. (5)

$$f_{osc} = \frac{N_u - (A_{si}f_{yi} + A_{ss}f_{ys})}{A_{so} + A_c} \quad (5)$$

where N_u = peak load in the test; f_{yi} and f_{ys} = yield strength of the inner steel tube and stiffeners, respectively; and A_{si}, A_{ss}, A_{so}, and A_c = areas of the inner steel tube, stiffeners, outer steel tube, and core concrete, respectively. Eq. (5) can be used to evaluate the interaction between the outer steel tube and sandwich concrete. The composite effect of the column would be stronger with an increase in the f_{osc} for the same material.

The values of f_{osc} of the specimens are presented in Fig. 13. As expected, f_{osc} increased with the increasing outer steel tube thickness due to the rise of nominal confinement factor for the same section size. Besides, f_{osc} of the UHPCFDST column was obviously smaller than that of the corresponding MUHPCFDST specimen. For instance, the f_{osc} of Specimens C203-4-76 and MC203-4-76 were 184.0 MPa and 200.3 (+7.86%) MPa, respectively. Also, the f_{osc} of Specimens C300-6-203A and MC300-6-203 were 207.1 MPa and 222.2 (+7.29%) MPa, respectively. It implies that the
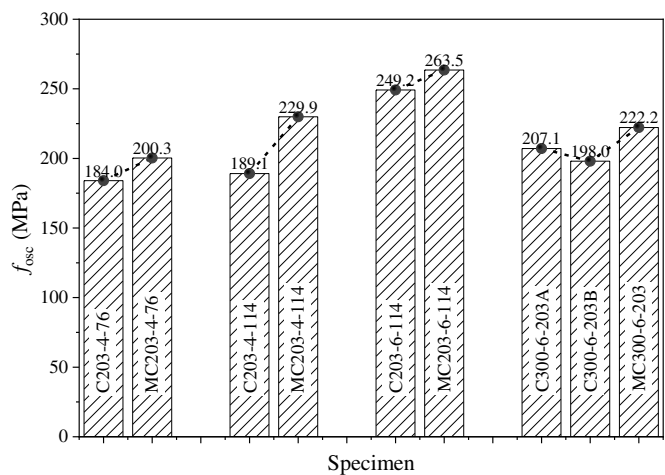
MUHPCFDST columns can utilize the strength of materials more efficiently than the UHPCFDST columns. However, since the material strength strongly influences the value of f_{osc}, more comparisons between different specimens need to be further conducted.

Strength Index

The strength index (SI) is also used to evaluate the composite effect of CFST members (Zhou et al. 2019). Generally, the larger the strength index is, the stronger the composite effect will be. SI is defined for columns as Eqs. (6) and (7), where N_u and N_0 are the experimental ultimate strength and superposed strength, respectively

$$SI = \frac{N_u}{N_0} \quad (6)$$

$$N_0 = A_c f_c + A_{so} f_{yo} + A_{si} f_{yi} + A_{ss} f_{ys} \quad (7)$$

SI of test columns are plotted in Fig. 14. It can be seen that SI of the UHPCFDST specimen was commonly less than that of the corresponding MUHPCFDST column, except Specimens C203-4-76 and MC203-4-76. SI of Specimen MC203-4-76 (1.229) was slightly less than that value of Specimen C203-4-6 (1.237), and one possible reason is that the nominal confinement factor of Specimen
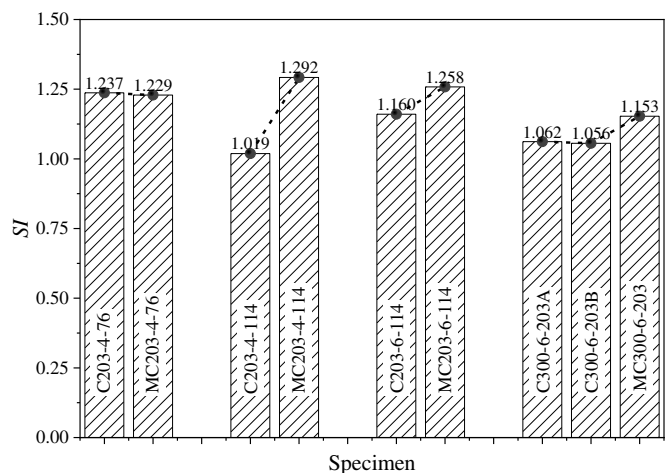

Fig. 14. Strength index of test columns.

MC203-4-76 (0.581) was less than that of Specimen C203-4-76 (0.663), as shown in Table 1. In general, stiffeners were available to increase the strength index and improve the utilization of material strength.

Ductility

Structural members need sufficient ductility to ensure serviceability under large ductile deformations, which may be caused by accidental actions. The residual resistance ratio (N_r/N_u) defined by Xiong (2012) was used to evaluate the ductility performance of the test columns, where N_r is the residual resistance corresponding to the limit axial shortening limit Δ_{lim}, which can be calculated by Eq. (8)

$$\Delta_{lim} = 0.5L\sqrt{\frac{f_y}{E_s}} \qquad (8)$$

where L = length of the column; and f_y and E_s = yield strength and elastic modulus of the outer steel tube, respectively.

To meet the ductility requirements, the residual resistance should not be less than the actions under the serviceability limit state. Xiong (2012) pointed out that the service load was up to 70% of the ultimate resistance according to the partial factors for actions and materials used in BS EN 1994-1-1 (EC 4) (CEN 2004) for gravity load combination. In other words, the residual resistance ratio should not be lower than 0.7 to ensure a safe design.

Fig. 15 illustrates the residual resistance ratio (N_r/N_u) of the test specimens. It can be found that for most specimens, the values of N_r/N_u were larger than 0.7. This means that these columns met the ductility requirements. However, the values of N_r/N_u for Specimens C300-6-203A and C300-6-203B were less than 0.7, attributing to their large hollow ratio (0.705). It should be mentioned that 0.705 was still less than the upper limit of 0.75 suggested by Han et al. (2019). This implies that the upper limit value of the hollow ratio of circular UHPCFDST may be more strict than circular CFDST with common strength material to meet the ductility requirements. Comparing Specimen C203-4-114 with Specimen C203-4-76, the hollow ratio increased from 0.390 to 0.585, while the residual resistance ratio decreased from 0.899 to 0.876, even though these two specimens had similar nominal confinement factors. A similar conclusion can be obtained by comparing Specimen MC203-4-114 with MC203-4-76. It implies that the residual resistance ratio decreased with the increase of the

Fig. 15. The residual resistance ratio of test columns.

hollow ratio. Then, it can be found that for the specimens with small outer tubes (203 mm in diameter), the residual resistance ratio of the UHPCFDST specimen and the corresponding MUHPCFDST specimen was similar owing to the small hollow ratio (less than 0.6). In addition, the resistance ratio of Specimen MC300-6-203 was 0.852, which was significantly larger than that (0.686) of Specimen C300-6-203A. This indicates that a larger upper limit hollow ratio can be used for circular MUHPCFDST columns compared with circular UHPCFDST columns.

Finite-Element Modeling and Parametric Study

FE Models

General Information
Three-dimensional FE models were developed using the software ABAQUS version 2021. The model consisted of two rigid plates, sandwich concrete, and steel components (including outer steel tube, inner steel tube, and stiffeners), as shown in Fig. 16(a). Four-node reduced shell elements (S4R) were used to simulate steel components, and eight-node reduced integral format 3D solid elements (C3D8R) were used to simulate sandwich concrete. A sweep meshing option was adopted, and typical meshes are shown in Figs. 16(b and c). Based on the mesh-sensitive analysis, elements with the dimension of 25 mm were appropriate to model steel tubes and concrete. Tao et al. (2011) pointed out that the effects of local imperfections and residual stresses were minimized by concrete filling. Therefore, these imperfections were ignored in FE models.

Material Modeling
Concrete. The concrete damaged-plasticity model in ABAQUS was used for the sandwich concrete. This paper proposed a new four-stage model to represent the strain hardening/softening of UHPC confined by steel tubes, as shown in Fig. 17. In the initial stage (from Point O to Point B), there is little interaction between UHPC and steel tubes. Therefore, the ascending branch of the stress-strain relationship of unconfined UHPC can be directly used to represent the curve OB until the peak strength f_c. Then, a plateau (from Point B to Point C) is included to represent the increased strain (corresponding to peak stress) of UHPC due to the confinement (Tao et al. 2013b). During this stage, the interaction between UHPC and steel tubes increases gradually. Beyond Point C, a softening stage is defined.

Yan (2005) proposed a model to describe the ascending curve OB. However, an apparent elastic stage was observed based on the uniaxial compressive test of the UHPC prism specimen (Wu et al. 2016; Al-Tikrite and Hadi 2017; Deng et al. 2020; Naeimi and Moustafa 2021). Therefore, a linear phase (from Point O to Point A) is defined to describe the elastic behavior of UHPC. Thus, the ascending curve OB can be described as follows:

$$\sigma_c = \begin{cases} \varepsilon E_c & 0 \le \varepsilon \le \varepsilon_e \\ f_e + (f_c - f_e)\dfrac{A\frac{\varepsilon-\varepsilon_e}{\varepsilon_0-\varepsilon_e} - \left(\frac{\varepsilon-\varepsilon_e}{\varepsilon_0-\varepsilon_e}\right)^2}{1 + (A-2)\frac{\varepsilon-\varepsilon_e}{\varepsilon_0-\varepsilon_e}} & \varepsilon \le \varepsilon_0 \end{cases} \qquad (9)$$

$$A = \frac{\varepsilon - \varepsilon_e}{f_c - f_e}E_c \qquad (10)$$

$$E_c = \frac{100,000}{1.484 + 120/f_c}\exp\left(\frac{9.3RI}{1,000}\right) \qquad (11)$$

$$\varepsilon_0 = 10^{-6}(1,683 + 13.347f_c)\exp(0.0008RI) \qquad (12)$$
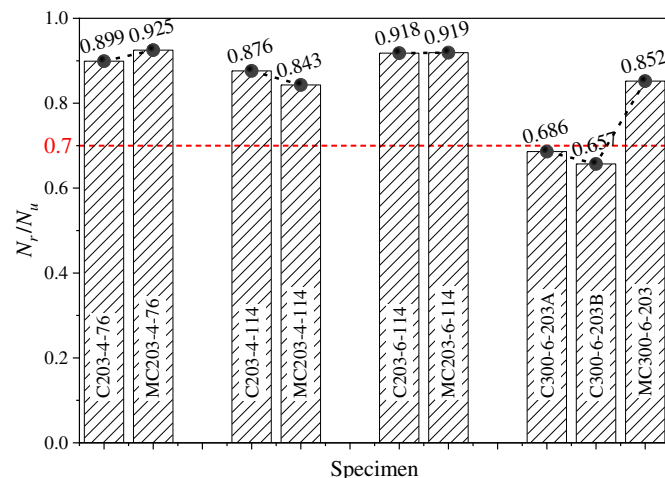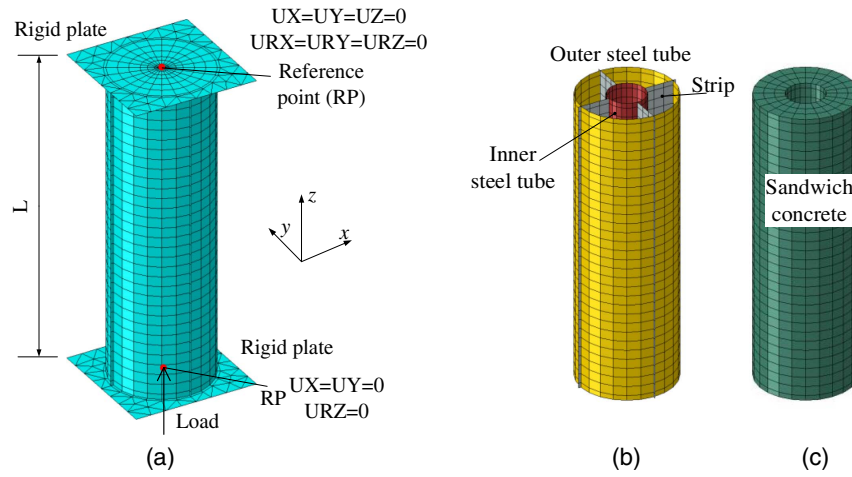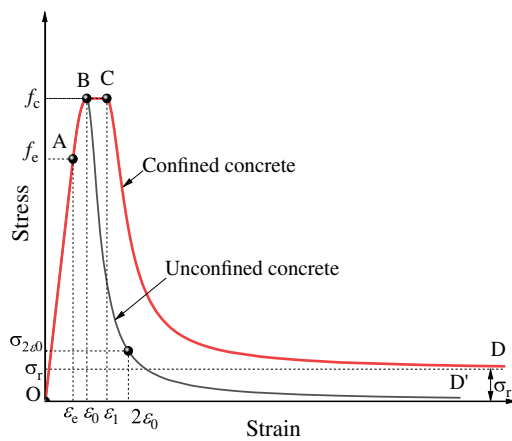
Fig. 16. Details of the FE model (MUHPCFDST): (a) FE model; (b) steel part; and (c) concrete part.

Fig. 17. Stress-strain model proposed for unconfined and confined concrete.

$$RI = V_f \frac{l_f}{d_f} \qquad (13)$$

where f_e = stress of UHPC at the end of the elastic stage, which can be taken as $0.8 f_c$; E_c = elastic modulus, which can be calculated by

Eq. (11); ε_0 = strain corresponding to the peak stress of UHPC under uniaxial compression, which can be calculated by Eq. (12); RI = fiber reinforcement index; and V_f, l_f, and d_f = volume content, length, and diameter of SF, respectively. Fig. 18 presents the comparisons of E_c and ε_0, which are predicted by different formulas (De Nicolo et al. 1994; ACI 2014; Guo et al. 2017; Yang et al. 2020). It can be found that Eqs. (11) and (12) have better predictions on the E_c and ε_0 of UHPC than other models.
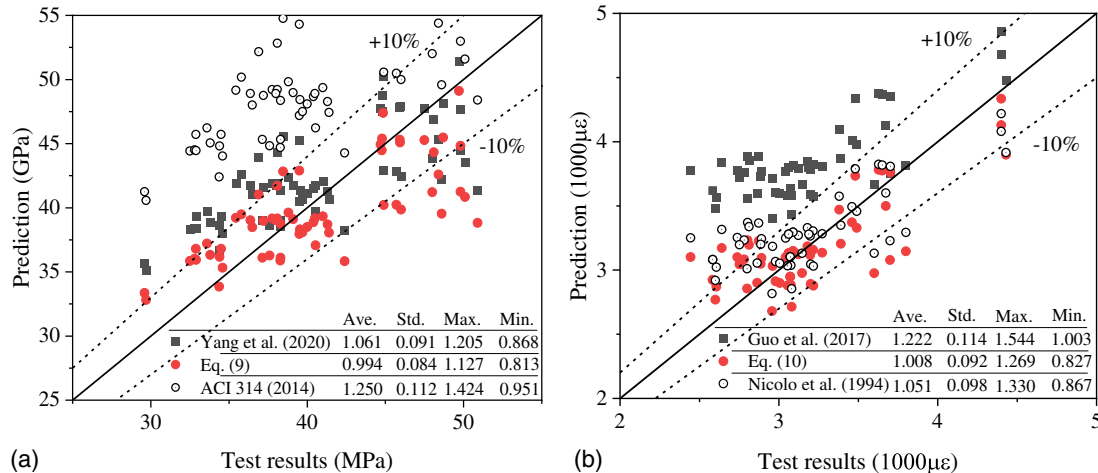
The strain at Point C (ε_1) is developed from the model proposed by Samani and Attard (2012), as shown in Eqs. (14)–(21)

$$\varepsilon_1 = \varepsilon_0 exp(k)k_\Omega \geq \varepsilon_0 \qquad (14)$$

$$k = (2.9224 - 0.00367 f_c)\left(\frac{f_r}{f_c}\right)^{0.3124+0.002 f_c} \qquad (15)$$

$$f_r = \begin{cases} p_0 k_\psi & \text{For CFDST column} \\ p_1 - p_0(1 - k_\psi) & \text{For MCFDST column} \end{cases} \qquad (16)$$

$$p_0 = \frac{2 t_o \sigma_{\theta,o}}{D_o - 2 t_o} \qquad (17)$$

Fig. 18. Tests results and predictions of E_c and ε_0: (a) elastic modulus E_c; and (b) strain at peak stress ε_0.
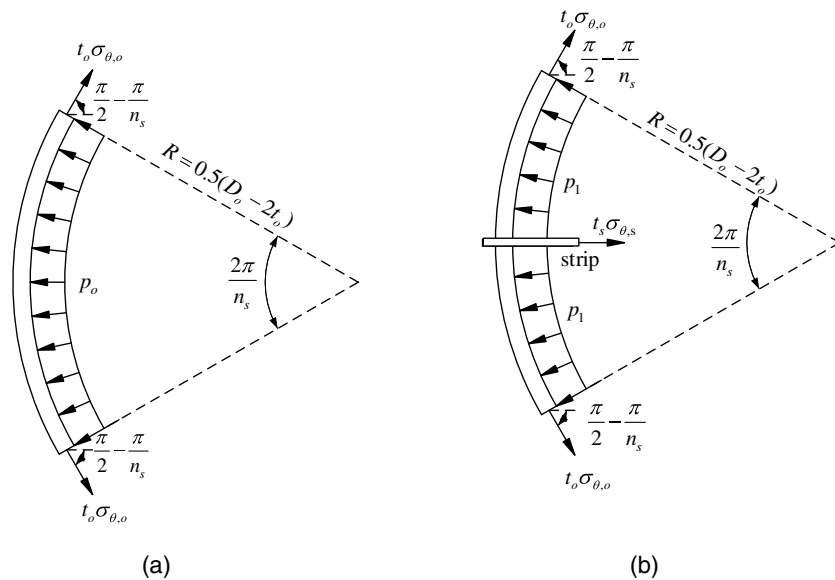
Fig. 19. Confining pressure from steel tube: (a) CFDST specimen; and (b) MCFDST specimen.

$$p_1 = \frac{2t_o\sigma_{\theta,o}\sin\frac{\pi}{n_s} + t_s\sigma_{\theta,s}}{(D_o - 2t_o)\left(\sin\frac{\pi}{n_s} - 0.5\sin^{-1}\frac{t_s}{R}\right)} \tag{18}$$

$$k_\Omega = 1.246\frac{A_c}{A_{ce}} \le 1 \tag{19}$$

$$k_\psi = \begin{cases} 1 & \psi' \le 125 \\ \max\left[0, min\left(\left(\frac{375}{\psi'}\right)^2, \sqrt{\frac{125}{\psi'}}\right)\right] & \psi' \le 125 \end{cases} \tag{20}$$

$$\psi' = \begin{cases} \dfrac{250}{f_y}\psi & n_s \le 2 \\ \dfrac{2}{n_s}\dfrac{250}{f_y}\psi & n_s > 2 \end{cases} \tag{21}$$

where k_Ω = section factor, which is used to quantify the impact of hollow ratio; f_r = confining stress corresponding to Point C in the concrete model, which can be calculated by Eqs. (16)–(18); p_0 and p_1 = confining pressure from steel tubes of CFDST and MCFDST specimens, respectively, as shown in Fig. 19; R = radius of sandwich concrete; n_s and t_s = quantity and thickness of the stiffener, respectively; and $\sigma_{\theta,o}$ and $\sigma_{\theta,s}$ = tensile transverse stress of the outer steel tube and stiffeners, respectively. It is not difficult to find that the value of p_1 increases with the increase of the stiffener quantity. According to Sakino et al. (2004), $\sigma_{\theta,o}$ can be taken as $0.19f_{yo}$. In this paper $\sigma_{\theta,s}$ can also be taken as $0.19f_{ys}$, where f_{yo} and f_{ys} are the yield strength of the outer tube and stiffeners, respectively.

For the descending branch of UHPC without confined (BD′), the rational formula suggested by GB 50010 (MOHURD 2010a) was used as follows:

$$\sigma_c = \frac{\varepsilon/\varepsilon_0}{m_c(\varepsilon/\varepsilon_0 - 1)^{n_c} + \varepsilon/\varepsilon_0}\varepsilon > \varepsilon_0 \tag{22}$$

$$\begin{cases} m_c = 2\left(\dfrac{f_c}{\sigma_{2\varepsilon_0}} - 1\right) \\ \dfrac{\sigma_{2\varepsilon_0}}{f_c} = 0.471(RI - 0.5) \le 0.5 \end{cases} \tag{23}$$

where m_c and n_c = parameters used to control the shape of the softening branch, and according to GB 50010 (MOHURD 2010a), n_c can be taken as 2; and $\sigma_{2\varepsilon_0}$ = stress corresponding to the strain at $2\varepsilon_0$ on the unconfinement stress-strain curve, as shown in Fig. 17. Besides, to avoid the value of m_c being too large, $0.1f_c$ can be defined as the lower limit for $\sigma_{2\varepsilon_0}$. Fig. 20 shows the experimental (Al-Tikrite and Hadi 2017; Deng et al. 2020; Naeimi and Moustafa 2021) and theoretical compressive stress-strain curves of UHPC without confinement. It can be seen that the proposed model can well describe the main characteristics of the compressive stress-strain curves from the test.

Whereas, for the descending branch of confined UHPC (CD), the modified rational formula based on Eq. (24) was used, which is defined as follows:

$$\sigma_c = \sigma_r + (f_c - \sigma_r)\frac{\varepsilon/\varepsilon_1}{m_c(\varepsilon/\varepsilon_1 - 1)^{n_c} + \varepsilon/\varepsilon_1} \tag{24}$$

$$\sigma_r = 0.7[1 - \exp(-1.38\xi)]\frac{A_c}{A_{ce}}f_c \le 0.25f_c \tag{25}$$

where σ_r = residual stress (see Fig. 17), and can be calculated by Eq. (25), which is developed from Tao et al. (2013b). A typical stress-strain curve of UHPC is used in the FE model, as shown in Fig. 21(a).

Additionally, tension stiffening was necessary to be defined in the FE model. Based on Tao et al. (2013b), the tensile strength f_t can be taken as 10% of the uniaxial compressive strength, and the fracture energy G_f can be calculated by Eq. (26) (Huang et al. 2020), where α_0 can be taken as 0.025 for UHPC

$$G_f = \alpha_0(f_c/10)^{0.7} \tag{26}$$

Steel. In the present study, the stress-strain model suggested by Tao et al. (2013a) was used to simulate the behavior of the steel component. A typical stress-strain curve of steel was used in the
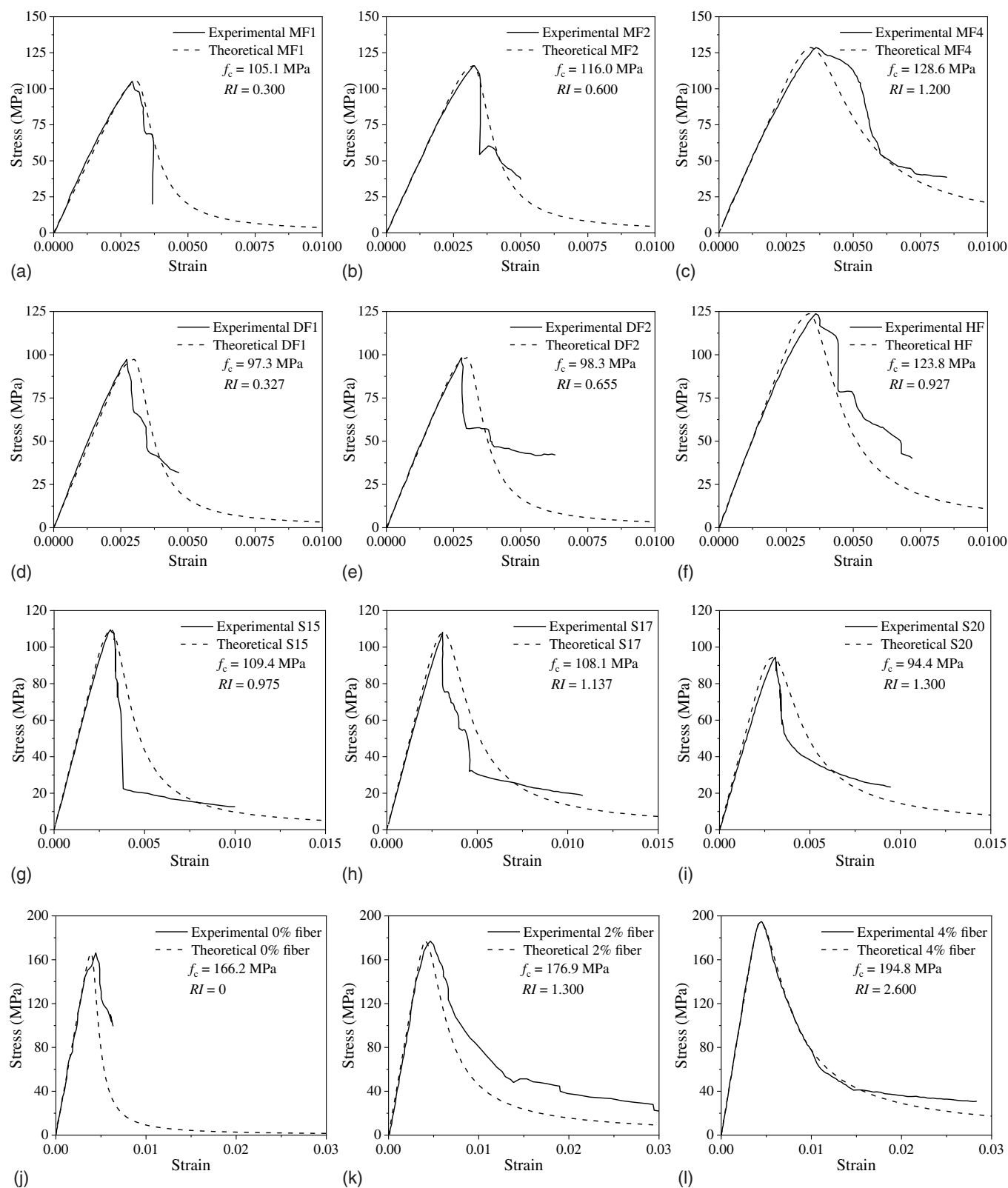
Fig. 20. Comparison between the empirical proposed model and experimental stress-strain curves: (a) MF1; (b) MF2; (c) MF4; (d) DF1; (e) DF2; (f) HF; (g) S15; (h) S17; (i) S20; (j) 0% fiber; (k) 2% fiber; and (l) 4% fiber. (a–f) (data from Al-Tikrite and Hadi 2017); (g–i) (data from Deng et al. 2020); and (j–l) (data from Naeimi and Moustafa 2021).

FE model illustrated in Fig. 21(b). However, considering that no plastic deformation was observed in any of the top and bottom plates during the test, the linear elastic material model was used to model the rigid plates.

Interactions and Boundary Conditions

The surface-to-surface contact was used to represent the interface between steel tubes and sandwich UHPC. The normal behavior of contact pairs was simulated by hard contact with the option *allow*
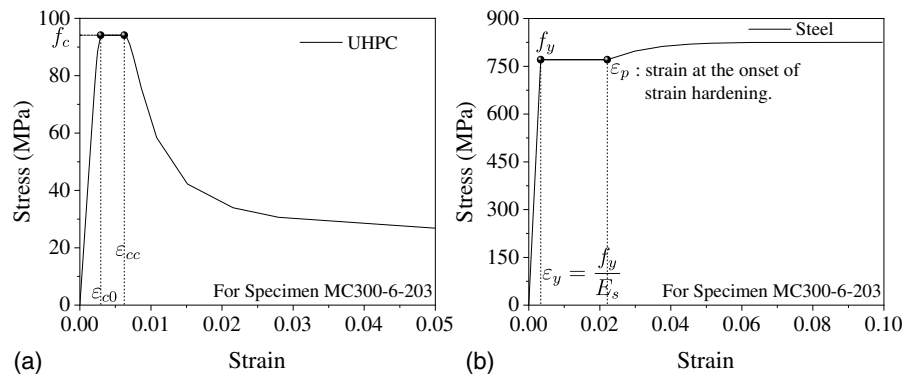
Fig. 21. Typical stress-strain curves of concrete and steel: (a) UHPC; and (b) steel.

Table 5. Influence of mesh density

Mesh label	Friction coefficient	Number of elements	Capacity (kN)	Calculation time (s)
Fine	0.3	25,889	12,448.7	2,307
Moderate	0.3	10,065	12,404.1	670
Coarse	0.3	4,293	12,330.2	310
Moderate	0.4	10,065	12,404.1	690
Moderate	0.5	10,065	12,405.6	630
Moderate	0.6	10,065	12,407.4	630

Fig. 22. Summary of mesh strategies ($\chi = 0.5$): (a) fine mesh; (b) moderate mesh; and (c) coarse mesh.

separation after contact, and the tangential behavior was simulated with the Coulomb friction model. Baltay and Gjelsvik (1990) indicated that the friction coefficient between steel and core concrete ranged from 0.3 to 0.6. According to Huang et al. (2019), a friction coefficient of 0.3 was adopted in this paper. The interaction between stiffeners and concrete was simulated by the *embedded* technology of ABAQUS to improve efficiency. Besides, as shown in Fig. 16(a), two reference points (RPs) were set at the centroids of the upper surface of the rigid top plate and the lower surface of the rigid bottom plate, respectively. Load and boundary conditions were directly applied to these two RPs (Zhou and Han 2019). The translational and rotational degrees of freedom were restrained at the top of the rigid plate to simulate the fixation, similar to the experiments. The bottom of the rigid plate was restrained in the direction of horizontal displacement to simulate the spherical hinge used in the test.

Sensitivity Analysis

Mesh Densities. Table 5 summarizes the data of three different mesh strategies shown in Fig. 22. Compared with the moderate meshing model, the increments of the ultimate bearing capacity of the coarse meshing model and fine meshing model were −73.9 kN (−0.6%) and 44.6 kN (+0.4%), respectively. It indicated that stable results could be achieved after refining to the moderate meshing density. Besides, the computational time of finer meshes increased dramatically. Thus, the moderate mesh was adopted in the following FE models to achieve computational efficiency.

Friction Coefficient. The influence of the friction coefficient was studied by varying the friction coefficients, as shown in Table 5. The maximum difference of the ultimate bearing capacity was 4.5 kN. It indicated that the friction coefficient hardly influenced the ultimate bearing capacity. Furthermore, a friction coefficient of 0.3 was adopted by Shen et al. (2022) and Lam et al. (2012). Therefore, it was also used in the following analyses.
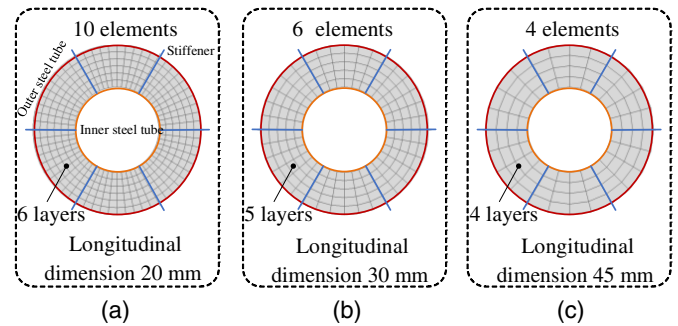
Model Verification

The results predicted by the FE model are summarized in Table 6. Comparing FE modeling results with experimental results, the respective average ratios of ultimate bearing capacity and the corresponding axial shortening are 0.970 and 0.945, respectively. The failure modes from FEM are illustrated in Fig. 23. Since that the geometry imperfection was ignored in the FE models, significant local buckling was not observed. Furthermore, the axial load-shortening curves of specimens from FE modeling and experimental results have been presented in Fig. 24. It can be seen that the FE modeling results are consistent with experimental results. Although there are some differences in the local positions, especially in the descending branch with significant axial shortening, the errors are still within the acceptable range.

Parametric Study

Four groups of FE models were designed to examine the influence of the governing parameters on the steel-concrete composite actions. The steel strength (f_y), concrete strength (f_c), hollow ratio (χ), stiffeners quantity (n_s), and variables of each parameter were summarized in Table 7. It is worth noting that for all the models, outer steel tube, inner steel tube, and stiffener were defined as the same material, with a thickness of 5 mm, and with a yield strength of f_y. Specimen length L was three times the outer steel tube's diameter D_o, and D_o was equal to ψt_o. Stiffeners were extended beyond the outer steel tube by 5 mm.

Effect of Steel Strength

As shown in Fig. 25(a), increasing the steel strength can significantly increase the ultimate bearing capacity (the peak load),

© ASCE

Table 6. Summary of experimental and FE results

Specimen	Δ_u (mm)	$\Delta_{u,FE}$ (mm)	$\dfrac{\Delta_{u,FE}}{\Delta_u}$	N_u kN	$N_{u,FE}$ (kN)	$\dfrac{N_{u,FE}}{N_u}$
C203-4-76	4.78	4.91	1.027	5,572.1	5,314.1	0.954
C203-4-114	4.02	3.71	0.923	4,751.4	4,683.7	0.986
C203-6-114	4.28	4.42	1.033	6,081.5	5,789.7	0.952
C300-6-203A	4.05	4.30	1.062	9,783.8	9,714.5	0.993
C300-6-203B	4.49	4.44	0.989	9,438.3	9,373.0	0.993
MC203-4-76	5.02	4.91	0.978	6,739.4	6,809.6	1.010
MC203-4-114	4.02	3.71	0.923	6,158.4	5,473.5	0.889
MC203-6-114	4.99	4.91	0.984	7,122.0	6,988.1	0.981
MC300-6-203	7.65	4.50	0.588	11,154.9	10,798.1	0.968
Average	—	—	0.945	—	—	0.970
Standard	—	—	0.134	—	—	0.034
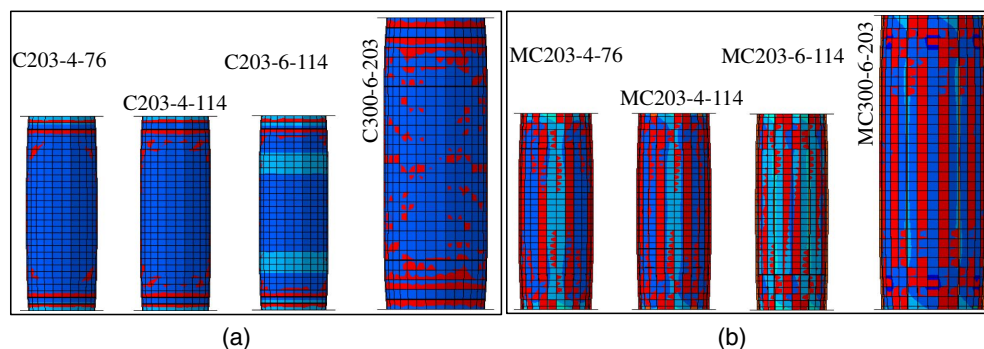
Fig. 23. FEM failure modes: (a) UHPCFDST columns; and (b) MUHPCFDST columns.

especially for specimens with six stiffeners. When the steel strength was increased from 460 MPa to 800 MPa, the respective peak load increment ratios were 36.5%, 27.2%, and 16.6% for specimens with diameter-to-thickness ratios as 62, 102, and 202. The concrete stress-axial strain curves (stress-strain curve and the concrete stress was the average stress of the sandwiched concrete) are illustrated in Fig. 26. Based on the definition, confinement factor ξ can be calculated by Eq. (27). When the diameter-to-thickness ratio ψ and concrete strength f_c were constants, the value of ξ increased with the increase of steel strength. A higher ξ commonly means a stronger steel-concrete composite action, and the strain corresponding to the peak point was also increased, as shown in Figs. 26(a and d). However, with the increase of ψ, the steel tube was more prone to buckling, which will reduce the confinement of sandwiched concrete from the steel tube. Therefore, there was little difference in the stress-strain curves for the specimen with a sizable diameter-to-thickness ratio, as shown in Figs. 26(c and f). The composite action between steel tube and concrete existed in the descending stage, so the stress-strain curves were still higher than the constitutive curve corresponding to plain concrete

$$\xi = \frac{4(\psi - 1)}{(\psi - 2)^2} \frac{f_y}{f_c} \tag{27}$$

Effect of Concrete Strength
As shown in Fig. 25(b), increasing the concrete strength can also increase the ultimate bearing capacity. The peak load increment ratio increased with the increase of diameter-to-thickness ratio ψ

because a larger ψ led to a larger concrete ratio (ratio between the area of concrete and the whole section). However, as shown in Eq. (27), ξ decreased with the increase of concrete strength f_c when the diameter-to-thickness ratio ψ and steel strength f_y were constants. Therefore, the steel-concrete composite action also decreased with the increase of concrete strength. It is evident that the strain corresponding to the peak point of the stress-strain curve (ε_p) was relative to the concrete strength, as shown in Fig. 27. When ψ was small (62), ε_p was reduced with increased concrete strength due to the decreased ξ. As shown in Fig. 27(a), when the concrete strength increased from 100 MPa to 200 MPa, ε_p decreased from 0.00818 to 0.00618 (about 24.4%). However, when ψ increased to 202, the small composite action between steel tube and concrete was reduced to so marginal that ε_p was mainly ascribed to the peak strain of the corresponding plain concrete. Thus, ε_p increased with the increase of concrete strength. As shown in Fig. 27(c), when concrete strength increased from 100 MPa to 200 MPa, ε_p increased from 0.00437 to 0.00496 (about 13.5%).

Effect of Hollow Ratio
The stress-strain curves of specimens with different hollow ratios χ are illustrated in Fig. 28. The hollow ratio had a negligible influence on the peak point of the concrete stress-axial strain curve. By contrast, it showed a significant effect on the descending stage. A larger hollow ratio would lead to a steeper descending stage, which may reduce the ductility of a specimen, especially for the specimen with a small diameter-to-thickness ratio ψ, as shown in Figs. 28(a and d). However, with the increase of ψ, the difference
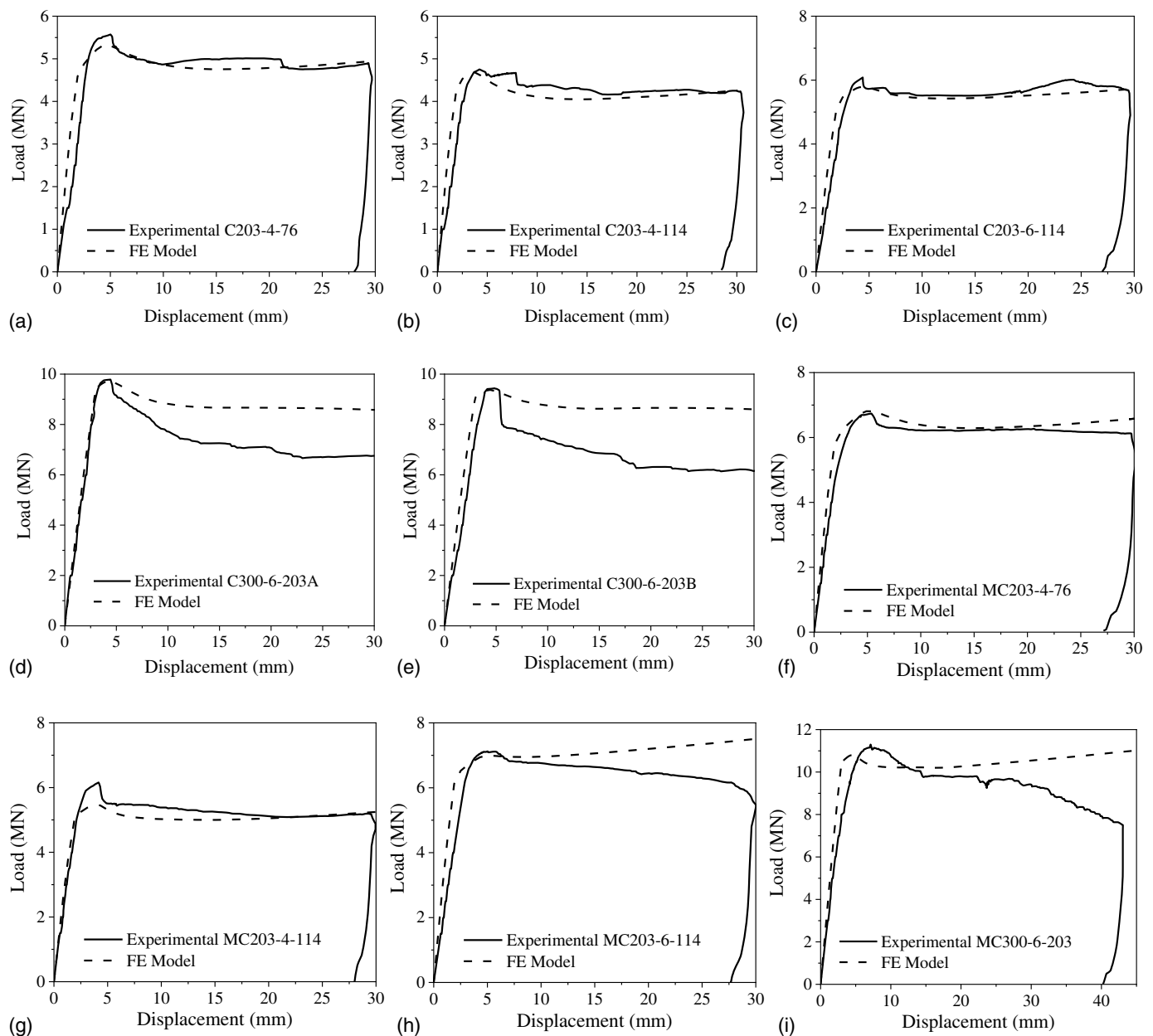
Fig. 24. Comparisons of load-axial shortening curves of specimens between FE modeling and experimental results: (a) C203-4-76; (b) C203-4-114; (c) C203-6-114; (d) C300-6-203A; (e) C300-6-203B; (f) MC203-4-76; (g) MC203-4-114; (h) MC203-6-114; and (i) MC300-6-203.

Table 7. Summary of variables of the parametric analysis

| Key parameter	Variables	f_y (MPa)	f_c MPa	χ	ψ	n_s
f_y	460,550,690,800	—	100,200	0.5	62,102,202	0,4,6
f_c	100,120,140,160,180,200	690	—	0.5	62,102,202	0,4,6
χ	0.25,0.4,0.5,0.6,0.75	690	100	—	62,102,202	0,4,6
n_s	0,3,4,6,8,12	690	100	0.5	62,102,202	—

between stress-strain curves was smaller and smaller, as caused by the decreasing confinement factor ξ. By comparing Figs. 28(a and d), it can also be found that the six stiffeners would greatly improve the stress-strain curve of the specimen. In other words, the additional stiffeners could enhance the composite effects between steel tubes and concrete.

Effect of Stiffeners Quantity

With the additional stiffeners, the ultimate bearing capacity of the specimen was increased. To evaluate the strength usage of stiffeners, a stiffener usage factor δ_s was defined as shown in Eq. (28). It is evident that the value of δ_s was not less than unity, and δ_s decreased with the increase of stiffeners quantity n_s, as shown
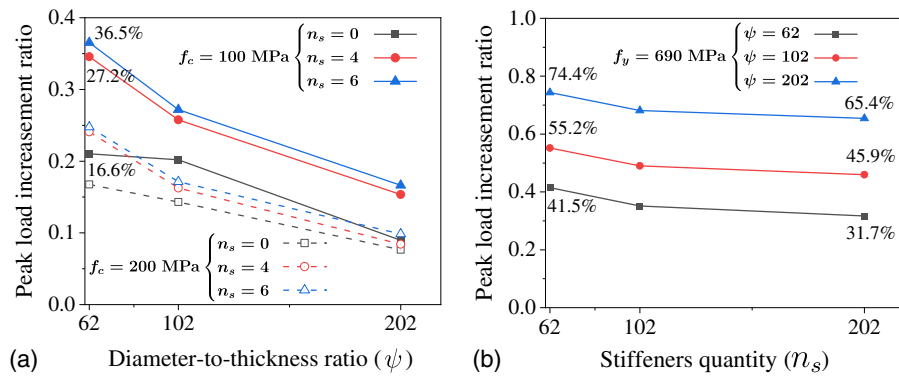
Fig. 25. Increment of peak load specimen with different parameters changed: (a) f_y from 460 MPa to 690 MPa; and (b) f_c from 100 MPa to 200 MPa.
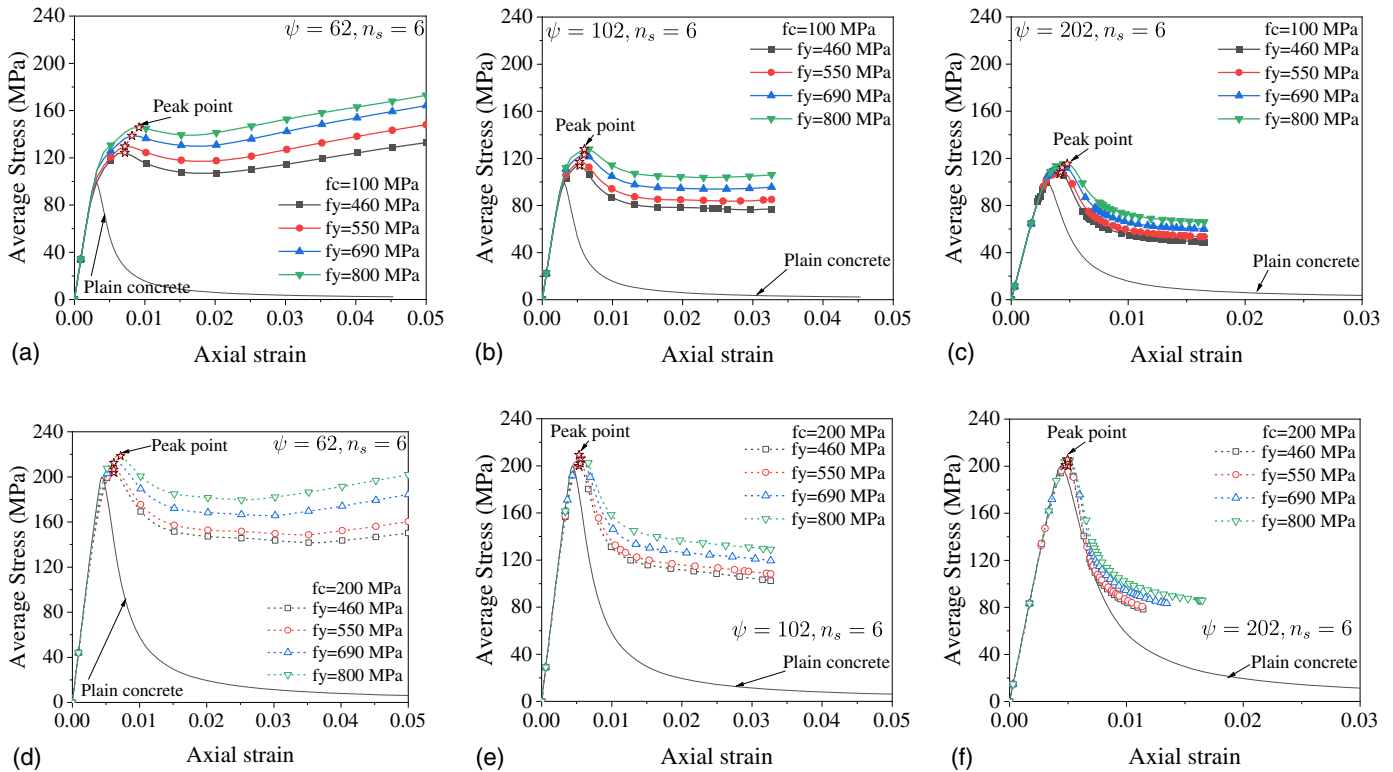
Fig. 26. Stress-strain curves of specimens with different steel strengths (f_y): (a) $D_o = 310\ mm$, $f_c = 100\ MPa$; (b) $D_o = 510\ mm$, $f_c = 100\ MPa$; (c) $D_o = 1,010\ mm$, $f_c = 100\ MPa$; (d) $D_o = 310\ mm$, $f_c = 200\ MPa$; (e) $D_o = 510\ mm$, $f_c = 200\ MPa$; and (f) $D_o = 1,010\ mm$, $f_c = 200\ MPa$.
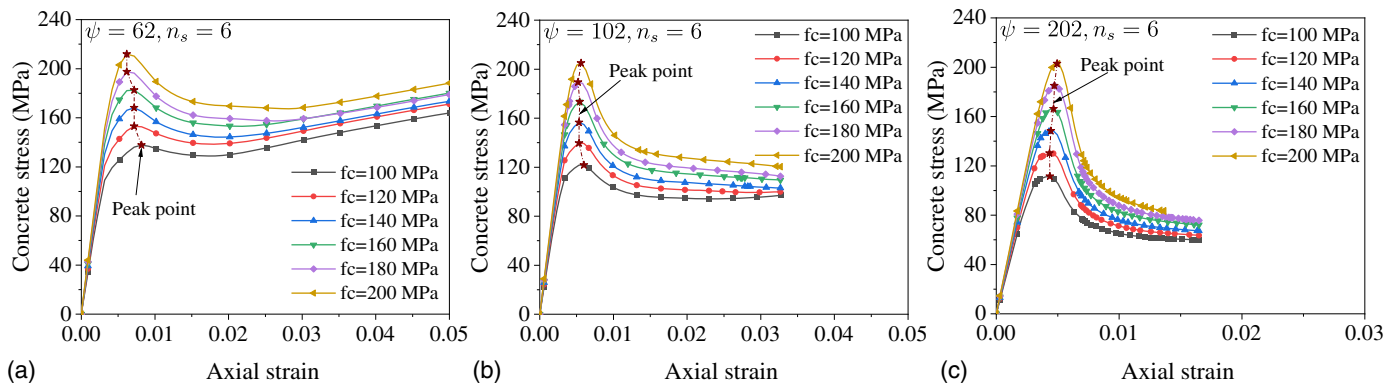
Fig. 27. Concrete stress-axial strain curves of specimens with different concrete strengths (f_c): (a) $D_o = 310\ mm$; (b) $D_o = 510\ mm$; and (c) $D_o = 1,010\ mm$.
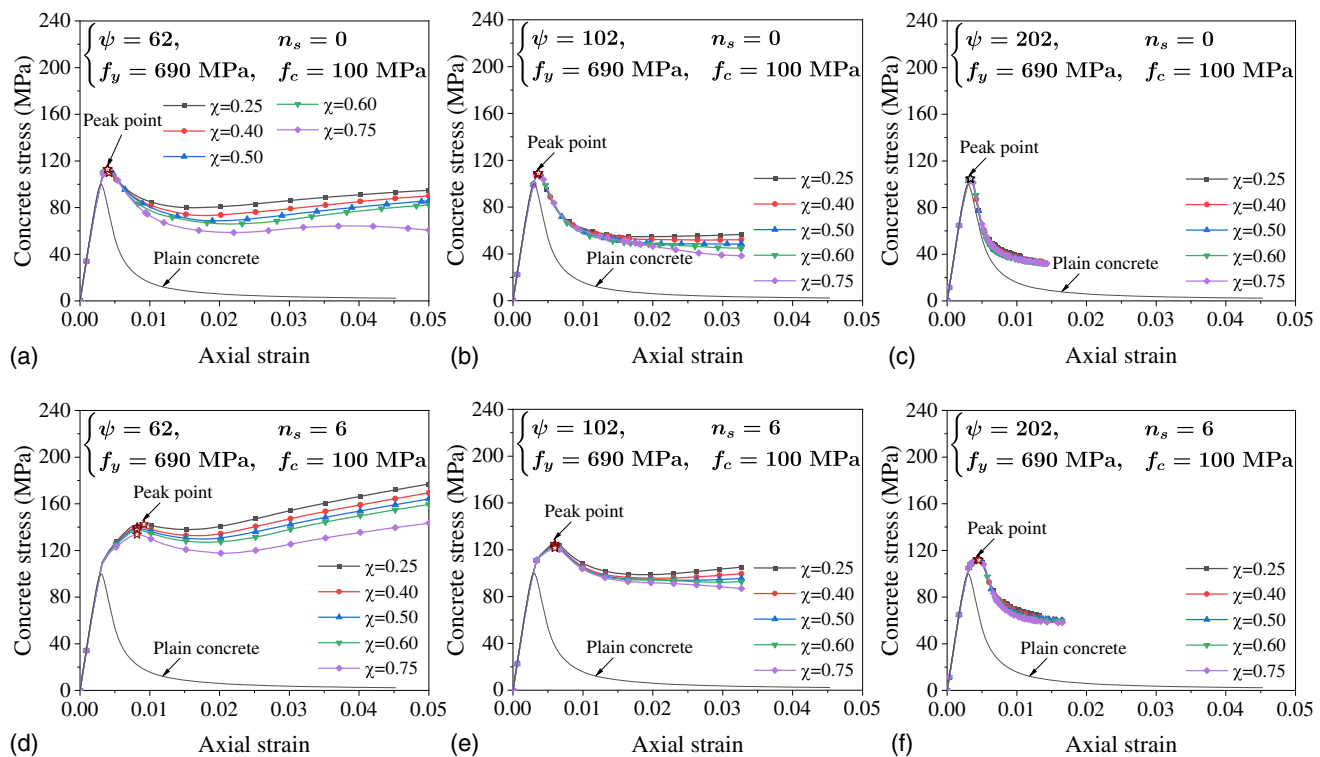
Fig. 28. Stress-strain curves of specimens with different hollow ratios (χ): (a) $D_o = 310$ mm, $n_s = 0$; (b) $D_o = 510$ mm, $n_s = 0$; (c) $D_o = 1,010$ mm, $n_s = 0$; (d) $D_o = 310$ mm, $n_s = 6$; (e) $D_o = 510$ mm, $n_s = 6$; and (f) $D_o = 1,010$ mm, $n_s = 6$.

in Fig. 29(a). Figs. 29(b and c) show the stress-strain curves of the specimens with different n_s. By comparing these curves, it can be found that the additional stiffeners could improve the steel-concrete composite effect efficiently, and the more stiffeners, the stronger the composite effect would be. By comparing Fig. 29(e) with Fig. 29(f), it can be found that adding stiffeners would effectively improve the stresses of concrete and improve the load-displacement curve of specimens

$$\delta_s = \frac{N_{ns} - N_0}{A_{ss}f_{ys}} \tag{28}$$

where N_{ns} = ultimate bearing capacity of specimens with n_s stiffeners; N_0 = capacity of the corresponding column without stiffener; and A_{ss} and f_{ys} = area and yield strength of stiffeners.

Design of Circular Concrete-Filled Steel Tubular Columns

Calculating method of a CFST column using T/CCES 7(CECS 2020), GB 50936 (MOHURD 2014), AISC 360-16 (AISC 2016), EC4 (CEN 2004), AIJ-2008 (AIJ 2008), AS/NZS 2327 (AS/NZS 2017), and CSA S16-19 (CAN/CSA 2019) are summarized in this section. Considering that all of these calculating methods are mainly used to predict the ultimate bearing capacity of CFST/CFDST columns, some slight modifications were made to consider contributions from the inner steel tube and stiffeners. It is noted that the superscripts are used to mark the values calculated from each design code, e.g., N_u^{GB} and $N_u^{GB'}$, where N_u^{GB} was the value calculated from design code GB 50936, while $N_u^{GB'}$ was the value including contribution from inner steel tube and stiffeners.

Limitations of Design Codes on Material Strength and Diameter-to-Thickness Ratio

As shown in Table 8, high-strength material has not been incorporated in current EC4, GB 50936, and T/CCES 7. In these design codes, the steel yield strength is only applicable up to 460 MPa. EC4 is only appropriate to concrete cylinder strength up to 60 MPa. GB 50936 and T/CCES 7 limit concrete strength to grade C80, with a cylinder strength of 70 MPa according to CEB-FIP (1993). A more extensive range of material strength is applicable in AISC 360-16 with a maximum steel yield strength of 525 MPa and concrete cylinder strength of 69 MPa, CSA S16-19 is applicable till a maximum steel yield strength of 690 MPa and concrete cylinder strength of 80 MPa, while in AIJ-2008, the respective maximum steel yield strength and concrete cylinder strength are 800 MPa and 90 MPa. High-strength materials are now recommended in AS/NZS 2327 with the upper limits for the strengths of concrete and steel being extended to 120 MPa (AS/NZS 2020) (cylinder strength) and 690 MPa (yield strength), respectively.

The limits and classification of the steel tube of CFST members subjected to axial compression loadings are summarized in Table 9. In EC4, T/CCES 7, GB 50936, AIJ-2008, and CSA S16-19, the maximum diameter-to-thickness ratio are $90\epsilon_k^2$, $100\epsilon_k^2$, $135\epsilon_k^2$, $146\epsilon_k^2$, and $119\epsilon_k^2$, respectively. The limits of diameter-to-thickness ratio given in AISC 360-16 and AS/NZS 2327 are the same ($264\epsilon_k^2$). It is worth noting that the slender section with the occurrence of local buckling is acceptable in both AISC 360-16 and AS/NZS 2327, while no specific provisions of other design codes are given for designing CFST columns with steel sections exceeding diameter-to-thickness ratios.
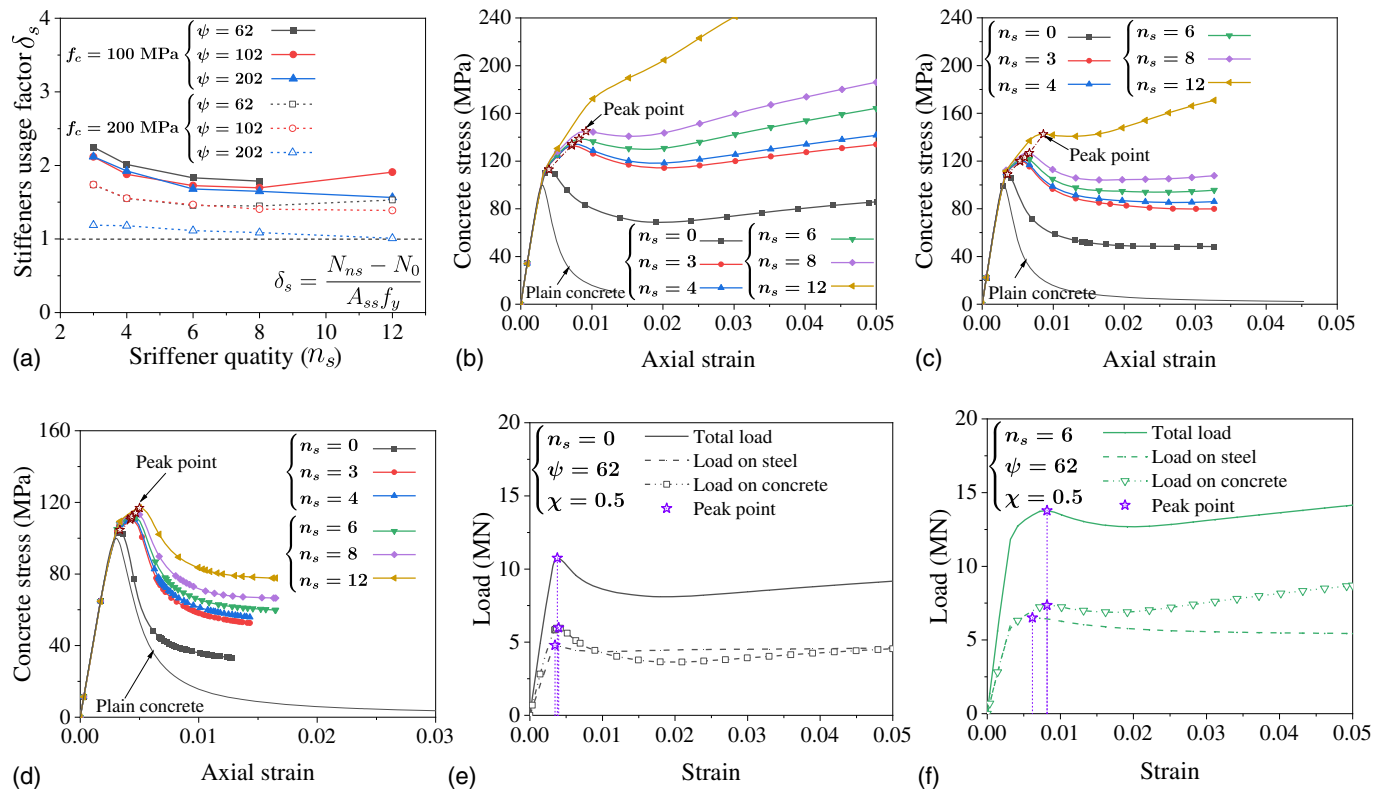
Fig. 29. Results of specimens with different stiffeners quantity (n_s): (a) stiffener usage factor δ_s; (b) stress-strain curve $\psi = 62$; (c) stress-strain curve $\psi = 102$; (d) stress-strain curve $\psi = 202$; (e) load-strain curve $n_s = 0$; and (f) load-strain curve $n_s = 6$.

Table 8. Material limits for the use of steel and concrete in CFST columns

Design code	Concrete strength (MPa)	Steel strength (MPa)
T/CCES 7	$40 \leq f_{cu} \leq 80$	$235 \leq f_y \leq 460$
GB 50936	$30 \leq f_{cu} \leq 80$	$235 \leq f_y \leq 460$
AISC 360-16	$21 \leq f_c' \leq 69$	$f_y \leq 525$
EC4	$20 \leq f_c' \leq 60$	$235 \leq f_y \leq 460$
AIJ-2008	$18 \leq f_c' \leq 90$	$f_y \leq 800$
AS/NZS 2327	$20 \leq f_c' \leq 120$	$f_y \leq 690$
CSA S16-19	$20 \leq f_c' \leq 80$	$f_y \leq 690$

Note: The recent amendment (AS/NZS 2327:2017 Amd 1:2020) extends the maximum strength of concrete from 100 to 120 MPa.

Calculation Methods in Existing Design Codes

T/CCES 7 Provisions

The calculation method of circular CFDST columns under axial compression is suggested by T/CCES 7, as shown in Eqs. (29) and (30). The compound axial compressive strength f_{osc} for the outer tube and sandwiched concrete is used to consider the enhancement effect due to the confinement effect. As shown in Eq. (30), this method also includes the effect of steel strength, concrete strength, and hollow ratio

$$N_u^{TC} = f_{osc}(A_{so} + A_c) + f_{yi}A_{si} \qquad (29)$$

Table 9. Limits of diameter-to-thickness ratio (D_o/t) for CFST columns

Design code	Elastic modulus (GPa)	Compact/ noncompact λ_p	Noncompact/ slender λ_r	Permitted limit	Limit for S690 steel
T/CCES 7	206	—	—	$100\epsilon_k^2$	34.1
GB 50936	206	—	—	$135\epsilon_k^2$	46.0
AISC 360-16	200	$0.15\dfrac{E_s}{f_y}$	$0.19\dfrac{E_s}{f_y}$	$0.31\dfrac{E_s}{f_y} = 264\epsilon_k^2$	89.9
EC4	210	—	—	$90\epsilon_k^2$	30.7
AIJ-2008	205	—	—	$0.171\dfrac{E_s}{f_y} = 146\epsilon_k^2$	49.7
AS/NZS 2327	200	$0.15\dfrac{E_s}{f_y}$	$0.19\dfrac{E_s}{f_y}$	$0.31\dfrac{E_s}{f_y} = 264\epsilon_k^2$	89.9
CSA S16-19	200	—	—	$119\epsilon_k^2$	40.5

Note: $\epsilon_k = \sqrt{235/f_y}$ is the steel grade correction factor.

where

$$\begin{cases} f_{osc} = C_1\chi^2 f_{yo} + C_2(1.14 + 1.02\xi)f_c \\ C_1 = \alpha/(1+\alpha) \\ C_2 = (1+\alpha_n)/(1+\alpha) \\ \alpha = A_{so}/A_c \\ \alpha_n = A_{so}/A_{ce} \end{cases} \quad (30)$$

in which α = steel ratio of outer steel tube; α_n = nominal steel ratio; ξ = nominal confinement factor; and χ = hollow ratio.

To predict the ultimate bearing capacity of MCFDST columns, the yield strength of stiffeners can be superimposed on N_u^{TC}, as follows

$$N_u^{TC'} = N_u^{TC} + f_{ys}A_{ss} \quad (31)$$

where f_{ys} and A_{ss} = yield strength and area of stiffeners, respectively.

GB 50936 Provisions

GB 50936 also proves a design method of circular CFST sections, as shown in Eqs. (32) and (33). The compound axial compressive strength f_{sc} of steel tube and core concrete is used to include the strength-enhancing effect from the steel-concrete composite behaviors

$$N_u^{GB} = f_{sc}(A_s + A_c) \quad (32)$$

where

$$f_{sc} = (1.12 + B\xi + C\xi^2)f_c \quad (33)$$

in which B and C = parameters relative to steel yield strength f_y and concrete strength f_c. For circular sections, values of B and C are summarized in Table 10.

This calculating method does not include the contribution of the inner steel tube and stiffeners. To predict the ultimate bearing capacity of CFDST/MCFDST columns, the yield strength of inner steel tube and stiffeners can be superimposed on N_u^{GB}, as shown in Eq. (34)

$$N_u^{TC'} = \begin{cases} N_u^{TC} + f_{yi}A_{si} & \text{For CFDST column} \\ N_u^{TC} + f_{yi}A_{si} + f_{ys}A_{ss} & \text{For MCFDST column} \end{cases} \quad (34)$$

where f_{ys} and A_{ss} = yield strength and area of stiffeners, respectively.

AISC 360-16 Provisions

In AISC 360-16, the calculation method for circular CFST columns under axial compression is divided into three parts according to the diameter-to-thickness ratio (see Table 9).
Compact Sections. For compact sections, the strength of circular CFST columns is calculated based on the strengths of concrete and steel components as

Table 10. Values of B and C

Section type	B	C
Solid	$0.176f_y/213 + 0.974$	$-0.104f_c/14.4 + 0.031$
Hollow	$0.106f_y/213 + 0.584$	$-0.037f_c/14.4 + 0.011$

$$N_u^{AIS} = A_s f_y + 0.95A_c f_c \quad (35)$$

Noncompact Sections. For noncompact sections, the compressive strength is calculated based on the values of N_p and N_y as

$$N_u^{AIS} = N_p - (N_p - N_y)\left(\frac{\lambda - \lambda_p}{\lambda_r - \lambda_p}\right)^2 \quad (36)$$

$$N_y = A_s f_y + 0.7A_c f_c \quad (37)$$

in which N_p and N_y are calculated by Eqs. (35) and (37), respectively; λ = slenderness ratio of section equal to diameter-to-thickness ratio, and the definitions of λ_p and λ_r are given in Table 9.
Slenderness Sections. For slenderness sections, the steel tube will experience local buckling when subjected to axial compression loadings. The compressive strength is calculated as

$$N_u^{AIS} = A_s f_{cr} + 0.7A_c f_c \quad (38)$$

$$f_{cr} = \frac{0.72f_y}{(D/t \cdot f_y/E_s)^{0.2}} \quad (39)$$

To predict the ultimate bearing capacity of CFDST/MCFDST columns, the yield strength of the inner steel tube and stiffeners can be superimposed on N_u^{AIS}, as shown in Eq. (40)

$$N_u^{AIS'} = \begin{cases} N_u^{AIS} + f_{yi}A_{si} & \text{For CFDST column} \\ N_u^{AIS} + f_{yi}A_{si} + f_{ys}A_{ss} & \text{For MCFDST column} \end{cases} \quad (40)$$

EC4 Provisions

The design method of circular CFST sections under axial compression in EC4, as shown in Eqs. (41) and (42), where the relative slenderness $\bar{\lambda} \le 0.5$, coefficients η_s and η_c represent the confinement effect, and L_e is the effective length of the CFST column

$$N_u^{EC} = \eta_s A_s f_y + A_c f_c\left(1 + \eta_c \frac{t}{D}\frac{f_y}{f_c}\right) \quad (41)$$

where

$$\begin{cases} \eta_s = 0.25(3 + 2\bar{\lambda}) \le 1 \\ \eta_c = 4.9 - 18.5\bar{\lambda} + 17\bar{\lambda}^2 \ge 0 \\ \bar{\lambda} = \sqrt{\dfrac{N_{cr}}{A_s f_y + A_c f_c}} \\ N_{cr} = \dfrac{\pi^2 (EI)_{eff}}{L_e^2} \\ (EI)_{eff} = E_s I_s + 0.6E_c I_c \end{cases} \quad (42)$$

To predict the ultimate bearing capacity of CFDST/MCFDST columns, the yield strength of the inner steel tube and stiffeners can be superimposed on N_u^{EC}, as shown in Eq. (43), and the stiffness of columns can be modified as Eq. (44)

$$N_u^{EC'} = \begin{cases} N_u^{EC} + f_{yi}A_{si} & \text{For CFDST column} \\ N_u^{EC} + f_{yi}A_{si} + f_{ys}A_{ss} & \text{For MCFDST column} \end{cases} \quad (43)$$

$$(EI)'_{eff} = \begin{cases} (EI)_{eff} + E_{si}I_{si} & \text{For CFDST column} \\ (EI)_{eff} + E_{si}I_{si} + E_{ss}I_{ss} & \text{For MCFDST column} \end{cases} \quad (44)$$

where E_s, E_{si}, and E_{ss} = elastic modulus for the outer steel tube, inner steel tube, and stiffeners, respectively; and I_s, I_{si},

and I_{ss} = second moments of area of outer steel tube, inner steel tube, and stiffeners, respectively.

AIJ-2008 Provisions
As shown in Eq. (45), the strength enhancement effect is simplified to the coefficient ϕ_c in AIJ-2008. For circular sections, the value is equal to 0.27

$$N_u^{AIJ} = (1 + \phi_c)A_s f_y + A_c f_c \tag{45}$$

To predict the ultimate bearing capacity of CFDST/MCFDST columns, the yield strength of the inner steel tube and stiffeners can be superimposed on N_u^{AIJ}, as shown in Eq. (46)

$$N_u^{AIJ'} = \begin{cases} N_u^{AIJ} + f_{yi}A_{si} & \text{For CFDST column} \\ N_u^{AIJ} + f_{yi}A_{si} + f_{ys}A_{ss} & \text{For MCFDST column} \end{cases} \tag{46}$$

AS/NZS 2327 Provisions
The calculating method provided by AS/NZS 2327 is similar to that in EC4. There are slight differences. For instance, local buckling is acceptable in AS/NZS 2327 and is considered in the form factor k_f using an effective width method. The compressive strength is calculated as

$$N_u^{As} = k_f \eta_s A_s f_y + A_c f_c \left(1 + \eta_c \frac{t}{D}\frac{f_y}{f_c}\right) \tag{47}$$

$$k_f = \frac{\pi(D_e - t)t}{A_s} \tag{48}$$

$$D_e = \min\left(\sqrt{\frac{\lambda_{ey}}{\lambda_p}}, \left(\frac{3\lambda_{ey}}{\lambda_p}\right)^2\right) \tag{49}$$

where

$$\begin{cases} \eta_s = 0.25(3 + 2\bar{\lambda}') \le 1 \\ \eta_c = 4.9 - 18.5\bar{\lambda} + 17\bar{\lambda}'^2 \ge 0 \\ \bar{\lambda}' = \sqrt{\dfrac{N_{cr}}{k_f A_s f_y + A_c f_c}} \\ N_{cr} = \dfrac{\pi^2(EI)_{eff}}{L_e^2} \\ (EI)_{eff} = E_s I_s + E_c I_c \end{cases} \tag{50}$$

in which λ_{ey} = element slenderness limit. For a concrete-filled circular steel tube, the value of λ_{ey} can be taken as 125.

To predict the ultimate bearing capacity of CFDST/MCFDST columns, the yield strength of the inner steel tube and stiffeners can be superimposed on N_u^{As}, as shown in Eq. (51), and the stiffness of columns can be rewritten as Eq. (44)

$$N_u^{As} = \begin{cases} N_u^{As} + f_{yi}A_{si} & \text{For CFDST column} \\ N_u^{As} + f_{yi}A_{si} + f_{ys}A_{ss} & \text{For MCFDST column} \end{cases} \tag{51}$$

CSA S16-19 Provisions
For circular CFST columns, the compressive strength is calculated as follows

$$N_u^{Cs} = \frac{\tau\phi A_s f_y + \tau'\alpha_1\phi_c A_c f_c}{(1 + \lambda^{2n})^{1/n}} \tag{52}$$

where

$$\begin{cases} \tau = 1/\sqrt{1 + \rho + \rho^2} \\ \tau' = 1 + \frac{25\rho^2\pi}{\frac{D}{t}}\frac{f_y}{\alpha_1 f_c} \\ \rho = 0.02(25 - D_o/L) \\ \lambda = \sqrt{N_p/N_{cr}} \\ \lambda = \sqrt{\frac{N_{cr}}{k_f A_s f_y + A_c f_c}} \\ N_{cr} = \frac{\pi^2(EI)_{eff}}{L_e^2} \\ (EI)_{eff} = E_s I_s + \frac{0.6E_c I_c}{1 + C_{fs}/C_f} \end{cases} \tag{53}$$

in which n can be taken as 1.8, C_{fs} and C_f are sustained axial load and the total load on the column, respectively. In this study, it is assumed that all the loads are sustained loads.

To predict the ultimate bearing capacity of CFDST/MCFDST columns, the yield strength of the inner steel tube and stiffeners can be superimposed on N_u^{Cs}, as shown in Eq. (54). The stiffness of columns can be revised as Eq. (44)

$$N_u^{Cs'} = \begin{cases} N_u^{Cs} + f_{yi}A_{si} & \text{For CFDST column} \\ N_u^{Cs} + f_{yi}A_{si} + f_{ys}A_{ss} & \text{For MCFDST column} \end{cases} \tag{54}$$

Proposed Calculation Method

As a new type of concrete, most of the current design codes have not accepted UHPC in the CFST columns yet. Only AS/NZS 2327 can provide the acceptable maximum strength of concrete as 120 MPa, as shown in Table 8. This means that the strength of concrete and steel used in this study (experiment and FE parametric analysis) has exceeded the acceptable range suggested by these design codes. Besides, local bucking is unacceptable by some design codes, such as T/CCES 7, GB 50936, EC4, and CSA S16-19. However, in this study, the diameter-to-thickness ratios of CFDST specimens exceeded the upper limitation suggested by these design codes, except Specimen C203-6-114. Furthermore, as described in the section "Calculation Methods in Existing Design Codes," calculating methods in the current design codes do not include the enhancement of stiffeners. It would underestimate the bearing capacity of MUHPCFDST members. Thus, the authors proposed a new calculation method to consider the improvement of stiffeners.

The bearing capacity of the CFDST/MCFDST column can be calculated by

$$N_u^p = \sigma_{cc}A_c + \sigma_{vo}A_{so} + \sigma_{vi}A_{si} + \sigma_{vs}A_{ss} \tag{55}$$

where N_u^p = predicted bearing capacity; A_c, A_{so}, A_{si}, and A_{ss} = areas of sandwich concrete, outer steel tube, inner steel tube, and stiffeners, respectively; σ_{vo} = vertical stress of the outer steel tube, and the value of σ_{vo} can be taken as the minimum of $0.89f_{yo}$ and $k_f f_{yo}$, where k_f was the form factor, calculated by Eq. (48); σ_{vs} and σ_{vi} = vertical stresses of stiffeners and inner steel tube, and the value can be taken as $0.89f_{yo}$ and f_{yi} respectively; and σ_{cc} = compressive strength of confined concrete. Mander et al. (1988) recommend Eq. (56) to calculate the value of σ_{cc} of column with normal strength material. Based on Eq. (56), Lu et al. (2021) proposed a modified formula [Eq. (57)] for UHPCFST columns, where f_r was the confining stress. As shown in the section "Material Modeling," Eqs. (17) and (18) can be used to calculate f_r of circular UHPCFDST and MUHPCFDST specimens, respectively. The enhancement from stiffeners (including the quantity of stiffener) is included in Eq. (18)

© ASCE

04021298-20

J. Struct. Eng.

$$\frac{\sigma_{cc}}{f_c} = -1.254 + 2.254\sqrt{1 + 7.94\frac{f_r}{f_c}} - 2\frac{f_r}{f_c} \qquad (56)$$

$$\frac{\sigma_{cc}}{f_c} = -2.354 + 3.354\sqrt{1 + 5.28\frac{f_r}{f_c}} - 2\frac{f_r}{f_c} \qquad (57)$$

Comparisons and Discussion

Circular UHPCFDST Columns

For the circular UHPCFDST specimens, the comparisons of the results from calculation methods in the existing design codes and FE/Test are summarized in Fig. 30(a). The average ratio of predictions of AISC 360-16 and CSA S16-19 were 0.767 and 0.894, respectively, which were conservative. The average ratio of predictions of T/CCES 7 and GB 50936 were 1.105 and 1.085, respectively, which were not safe. By contrast, the predictions from AS/NZS 2327-2017, AIJ-2008, and EC 4 were close to the FEM/test results, and the average ratios are 1.006, 1.021, and 1.033, respectively. The predictions from the proposed method also showed good accuracy, with an average error of −1.9%. In other words, the proposed method and calculating methods in AS/NZS 2327-2017, AIJ-2008, and EC 4 can predict the bearing capacity of circular UHPCFDST short columns.
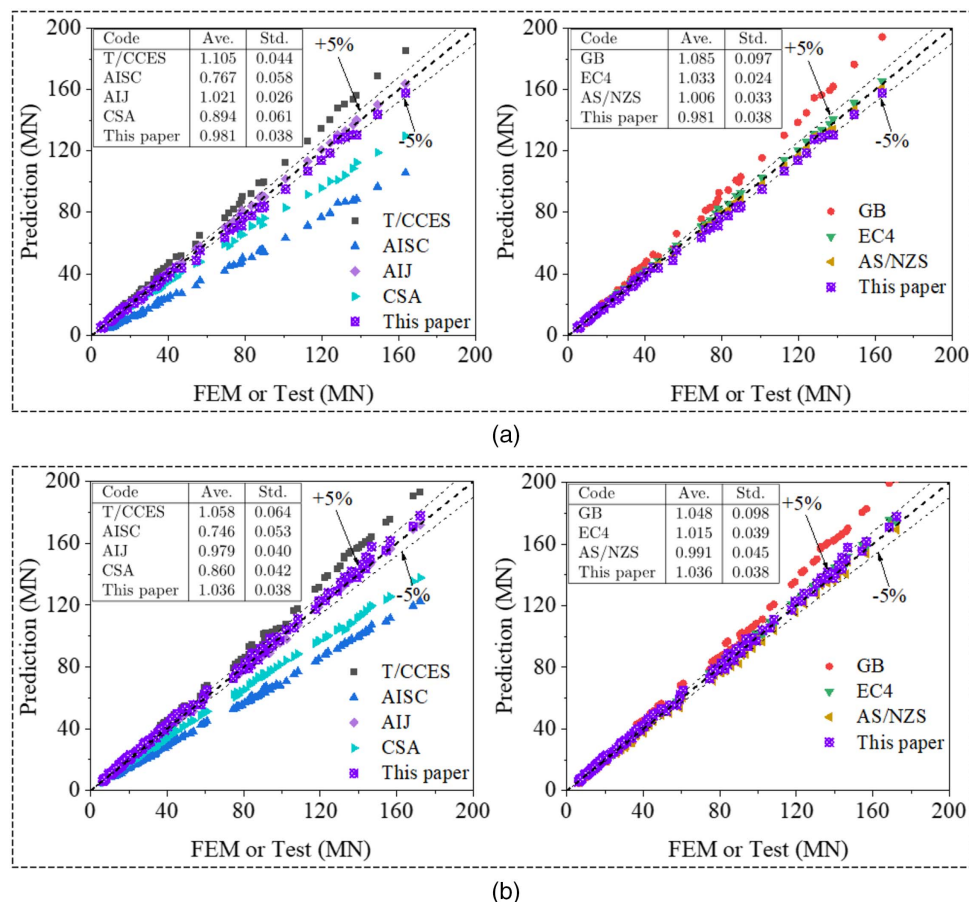
Circular MUHPCFDST Columns

Fig. 30(b) illustrates the comparisons of the results from calculation methods in the existing design codes and FE/Test. Similar to that of

the UHPCFDST columns, predictions of ACI-2014 (ACI 2014) and CSA S16-19 were also conservative. The average ratio of predictions of T/CCES 7 and GB 50936 was slightly higher than the FEM/Test results, especially for the specimens with a large capacity. The predictions from AIJ-2008, EC4, and AS/NZS 2327 were very close to the FEM/test results: the average ratios were between 0.979 and 1.015, and the coefficients of variation were also smaller than 0.05. Furthermore, the proposed method also showed good accuracy: the average ratio and coefficients of variation were 1.036 and 0.038, respectively. Both effects from local buckling and stiffeners were considered in the proposed method. However, compared with that of UHPCFDST columns, the average ratio of predictions of MUHPCFDST columns from AIJ-2008, EC4, and AS/NZS 2327 was reduced by 1.5%–4.1%. In general, the proposed method and calculating methods in AIJ-2008, EC 4, and AS/NZS 2327 can also predict the ultimate bearing capacity of the circular MUHPCFDST column well.

Conclusion

This paper presents an experimental study and numerical analysis of the axial behavior of the circular UHPCFDST and MUHPCFDST stub columns. Based on the test results and discussion in this paper, the following conclusions can be drawn:

1. Sandwich concrete in circular UHPCFDST specimens suffered oblique cracking, whereas the concrete in circular MUHPCFDST specimens experienced crushing.

Fig. 30. Comparison of predictions from different methods for UHPCFDST and MUHPCFDST columns: (a) UHPCFDST columns; and (b) MUHPCFDST columns.

2. Stiffeners significantly alleviated the load dropping phenomenon in the descending branch. Besides, stiffeners were also helpful to increase the strength index, and the average increment ratio was 10.47%.

3. All the circular MUPHCFDST specimens met the ductility requirements. However, the residual resistance ratios of the circular UHPCFDST specimen with large hollow ratios (0.705) were slightly less than 0.7, which did not meet the ductility requirements. The upper limit of the hollow ratio of circular UHPCFDST should be reduced based on the current value for the traditional CFDST column.

4. A uniaxial stress-strain function of UHPC under compression was developed and then used in modeling the UHPCFDST and MUHPCFDST columns. The predictions from the new FE model were compared with the experimental results, which indicated that the new FE model was available for simulating the axial behavior of the circular UHPCFDST and MUHPCFDST stub columns.

5. The proposed calculation method and calculating methods in AS/NZS 2327, AIJ-2008, and EC4 introduce the contribution of the inner steel tube and stiffeners to the section "Calculation Methods in Existing Design Codes" can predict the axial compressive bearing capacity of circular UHPCFDST and MUHPCFDST stub columns well.

It is worth noting that when calculating the contact pressure between steel and concrete, it was assumed that the stiffener was thin with a thickness not greater than the outer steel tube's thickness t_o. For thick stiffeners, further studies on the contact pressure between steel and concrete are necessary. Besides, the results from this study were mainly applicable to high-strength material: for concrete, the range of cylinder strength was 100–200 MPa; and for steel, the range of yield strength was 460–800 MPa.

Data Availability Statement

All data, models, and code generated or used during the study appear in the published article.

Acknowledgments

References

ACI (American Concrete Institute). 2014. *Building code requirements for structural concrete and commentary.* ACI 318-14. Chicago: ACI.

Ahmed, M., Q. Q. Liang, V. I. Patel, and M. N. S. Hadi. 2019a. "Local-global interaction buckling of square high strength concrete-filled double steel tubular slender beam-columns." *Thin Walled Struct.* 143 (Oct): 106244. https://doi.org/10.1016/j.tws.2019.106244.

Ahmed, M., Q. Q. Liang, V. I. Patel, and M. N. S. Hadi. 2019b. "Numerical analysis of axially loaded circular high strength concrete-filled double steel tubular short columns." *Thin Walled Struct.* 138 (May): 105–116. https://doi.org/10.1016/j.tws.2019.02.001.

AIJ (Architectural Institute of Japan). 2008. *Recommendations for design and construction of concrete filled steel tubular structures.* Tokyo: AIJ.

AISC (American Institute of Steel Construction). 2016. *Specification for structural steel buildings.* ANSI/AISC 360. Chicago: AISC.

Alqawzai, S., K. Chen, L. Shen, M. Ding, B. Yang, and M. Elchalakani. 2020. "Behavior of octagonal concrete-filled double-skin steel tube stub columns under axial compression." *J. Constr. Steel Res.* 170 (Jul): 106115. https://doi.org/10.1016/j.jcsr.2020.106115.

Al-Tikrite, A., and M. N. S. Hadi. 2017. "Mechanical properties of reactive powder concrete containing industrial and waste steel fibres at different ratios under compression." *Constr. Build. Mater.* 154 (Nov): 1024–1034. https://doi.org/10.1016/j.conbuildmat.2017.08.024.

AS/NZS (Australian/New Zealand Standard). 2017. *Composite structures—Composite steel-concrete construction in buildings.* AS/NZS 2327-2017. Sydney, Australia: AS/NZS.

AS/NZS (Australian/New Zealand Standard). 2020. *Composite structures—Composite steel-concrete construction in buildings.* AS/NZS 2327:2017 Amd 1:2020. Sydney, Australia: AS/NZS.

ASTM. 1999. *Standard test method for compressive strength of cylindrical concrete specimens.* ASTM C39/C39M-99. West Conshohocken, PA: ASTM.

Ayough, P., N. H. R. Sulong, and Z. Ibrahim. 2020. "Analysis and review of concrete-filled double skin steel tubes under compression." *Thin Walled Struct.* 148 (Mar): 106495. https://doi.org/10.1016/j.tws.2019.106495.

Baltay, P., and A. Gjelsvik. 1990. "Coefficient of friction for steel on concrete at high normal stress." *J. Mater. Civ. Eng.* 2 (1): 46–49. https://doi.org/10.1061/(ASCE)0899-1561(1990)2:1(46).

Cai, H., L. H. Xu, Y. Chi, Y. X. Yan, C. L. Yu, and C. L. He. 2021a. "Seismic performance of rectangular ultra-high performance concrete filled steel tube (UHPCFST) columns." *Compos. Struct.* 259 (Mar): 113242. https://doi.org/10.1016/j.compstruct.2020.113242.

Cai, Y. C., M. N. Su, X. R. Chen, and Y. Ben. 2021b. "High strength steel square and rectangular tubular stub columns infilled with concrete." *J. Constr. Steel Res.* 179 (Apr): 106536. https://doi.org/10.1016/j.jcsr.2021.106536.

CAN/CSA (Canadian Standards Association). 2019. *Design of steel structures.* CSA S16-19. Toronto: CAN/CSA.

CEB-FIP (Comité Euro-International du Béton-Fédération Internationale de la Précontrainte). 1993. *CEB-FIP model code 1990.* London: CEB-FIP.

CECS (China Association for Engineering Construction Standardization). 2020. *Technical specification for concrete-filled double skin steel tubular structures.* T/CCES 7-2020. Beijing: CECS.

CEN (European Committee for Standardization). 2004. *Design of steel and concrete structures—Part 1-1: General rules and rules for building.* BS EN 1994-1-1, Eurocode 4. Chicago: CEN.

Chen, S. M., R. Zhang, L. J. Jia, J. Y. Wang, and P. Gu. 2018. "Structural behavior of UHPC filled steel tube columns under axial loading." *Thin Walled Struct.* 130 (Sep): 550–563. https://doi.org/10.1016/j.tws.2018.06.016.

Chu, H. Y., Y. Zhang, F. J. Wang, T. T. Feng, L. G. Wang, and D. Q. Wang. 2020. "Effect of graphene oxide on mechanical properties and durability of ultra-high-performance concrete prepared from recycled sand." *Nanomaterials (Basel)* 10 (9): 1718. https://doi.org/10.3390/nano10091718.

Deng, F. Q., L. H. Xu, Y. Chi, F. H. Wu, and Q. Chen. 2020. "Effect of steel-polypropylene hybrid fiber and coarse aggregate inclusion on the stress-strain behavior of ultra-high performance concrete under uniaxial compression." *Compos. Struct.* 252 (Nov): 112685. https://doi.org/10.1016/j.compstruct.2020.112685.

De Nicolo, B., L. Pani, and E. Pozzo. 1994. "Strain of concrete at peak compressive stress for a wide range of compressive strengths." *Mater. Struct.* 27 (4): 206–210. https://doi.org/10.1007/BF02473034.

Ding, M. 2020. "Experimental study on the mechanical behavior of multicavity concrete filled double skin steel tubular stub columns under axial compression loads." M.E. thesis, School of Civil Engineering, Chongqing Univ.

Ding, M., L. Shen, and B. Yang. 2019. "FE simulation of a new type of concrete-filled double skin steel tube with stiffeners." In *Proc., 16th East Asia-Pacific Conf. on Structural Engineering and Construction (EASEC16)*, edited by C. M. Wang, V. Dao, and S. Kitipornchai. Berlin: Springer. https://doi.org/10.1007/978-981-15-8079-6_159.

Dong, C. X., and J. C. M. Ho. 2013. "Improving interface bonding of double-skinned CFST columns." *Mag. Concr. Res.* 65 (20): 1199–1211. https://doi.org/10.1680/macr.13.00041.

Duarte, A. P. C., B. A. Silva, N. Silvestre, J. de Brito, E. Julio, and J. M. Castro. 2016. "Tests and design of short steel tubes filled with rubberised concrete." *Eng. Struct.* 112 (Apr): 274–286. https://doi.org/10.1016/j.engstruct.2016.01.018.

Ekmekyapar, T., O. H. Alwan, H. G. Hasan, B. A. Shehab, and B. J. M. Al-Eliwi. 2019. "Comparison of classical, double skin and double section CFST stub columns: Experiments and design formulations." *J. Constr. Steel Res.* 155 (Apr): 192–204. https://doi.org/10.1016/j.jcsr.2018.12.025.

Elchalakani, M., M. F. Hassanein, A. Karrech, S. Fawzia, B. Yang, and V. I. Patel. 2018. "Experimental tests and design of rubberised concrete-filled double skin circular tubular short columns." *Structures* 15 (Aug): 196–210. https://doi.org/10.1016/j.istruc.2018.07.004.

Fang, X. D., and S. J. Lin. 2014. "Axial compressive test of columns with multi barrel tube-confined high performance concrete." [In Chinese.] *J. Build. Struct.* 35 (4): 236–245. https://doi.org/10.14006/j.jzjgxb.2014.04.031.

Farahi, M., A. Heidarpour, X. L. Zhao, and R. Al-Mahaidi. 2017. "Effect of ultra-high strength steel on mitigation of non-ductile yielding of concrete-filled double-skin columns." *Constr. Build. Mater.* 147 (Aug): 736–749. https://doi.org/10.1016/j.conbuildmat.2017.04.189.

Graybeal, B. A. 2007. "Compressive behavior of ultra-high-performance fiber-reinforced concrete." *ACI Mater. J.* 104 (2): 146–152. https://doi.org/10.1016/j.compstruct.2018.07.102.

Guo, X. Y., J. F. Kang, and J. S. Zhu. 2017. "Constitutive relationship of ultrahigh performance concrete under uni-axial compression." [In Chinese.] *J. Southeast Univ. (Nat. Sci. Ed.)* 47 (2): 369–376. https://doi.org/10.3969/j.issn.1001-0505.2017.02.028.

Habel, K., M. Viviani, E. Denarie, and E. Bruehwiler. 2006. "Development of the mechanical properties of an ultra-high performance fiber reinforced concrete (UHPFRC)." *Cem. Concr. Res.* 36 (7): 1362–1370. https://doi.org/10.1016/j.cemconres.2006.03.009.

Han, L. H., H. Huang, Z. Tao, and X. L. Zhao. 2006. "Concrete-filled double skin steel tubular (CFDST) beam-columns subjected to cyclic bending." *Eng. Struct.* 28 (12): 1698–1714. https://doi.org/10.1016/j.engstruct.2006.03.004.

Han, L. H., H. Huang, and X. L. Zhao. 2009. "Analytical behaviour of Concrete-filled Double Skin Steel Tubular (CFDST) beam-columns under cyclic loading." *Thin Walled Struct.* 47 (6): 668–680. https://doi.org/10.1016/j.tws.2008.11.008.

Han, L. H., D. Lam, and D. A. Nethercot. 2019. *Design guide for concrete-filled double skin steel tubular structures.* Boca Raton, FL: CRC Press/Taylor & Francis.

Han, L. H., and Z. Tao. 2001. "Study on behavior of concrete filled square steel tubes under axial load." [In Chinese.] *China Civ. Eng. J.* 34 (2): 17–25.

Hasan, H. G., and T. Ekmekyapar. 2019. "Mechanical performance of stiffened concrete filled double skin steel tubular stub columns under axial compression." *KSCE J. Civ. Eng.* 23 (5): 2281–2292. https://doi.org/10.1007/s12205-019-1313-6.

Hsiao, P., K. K. Hayashi, R. Nishi, X. Lin, and M. Nakashima. 2015. "Investigation of concrete-filled double-skin steel tubular columns with ultrahigh-strength steel." *J. Struct. Eng.* 141 (7): 04014166. https://doi.org/10.1061/(ASCE)ST.1943-541X.0001126.

Huang, W., Z. C. Fan, P. L. Shen, L. N. Lu, and Z. Zhou. 2020. "Experimental and numerical study on the compressive behavior of micro-expansive ultra-high-performance concrete-filled steel tube columns." *Constr. Build. Mater.* 254 (Sep): 119150. https://doi.org/10.1016/j.conbuildmat.2020.119150.

Huang, Z. C., D. X. Li, B. Uy, H. T. Thai, and C. Hou. 2019. "Local and post-local buckling of fabricated high-strength steel and composite columns." *J. Constr. Steel Res.* 154 (Mar): 235–249. https://doi.org/10.1016/j.jcsr.2018.12.004.

Kang, S. T., Y. Lee, Y. D. Park, and J. K. Kim. 2010. "Tensile fracture properties of an ultra high performance fiber reinforced concrete (UHPFRC) with steel fiber." *Compos. Struct.* 92 (1): 61–71. https://doi.org/10.1016/j.compstruct.2009.06.012.

Khusru, S., S. Fawzia, D. P. Thambiratnam, and M. Elchalakani. 2020. "A parametric study: High performance double skin tubular column using rubberised concrete." *Compos. Struct.* 235 (Mar): 111741. https://doi.org/10.1016/j.compstruct.2019.111741.

Krahl, P. A., G. d. M. Saleme Gidrao, and R. Carrazedo. 2019. "Cyclic behavior of UHPFRC under compression." *Cem. Concr. Compos.* 104 (Nov): 103363. https://doi.org/10.1016/j.cemconcomp.2019.103363.

Lam, D., X. H. Dai, L. H. Han, Q. X. Ren, and W. Li. 2012. "Behaviour of inclined, tapered and STS square CFST stub columns subjected to axial load." *Thin Walled Struct.* 54 (Nov): 94–105. https://doi.org/10.1016/j.tws.2012.02.010.

Li, W., and Y. X. Cai. 2019. "Performance of CFDST stub columns using high-strength steel subjected to axial compression." *Thin Walled Struct.* 141 (Aug): 411–422. https://doi.org/10.1016/j.tws.2019.04.021.

Li, Y. L., X. L. Zhao, R. K. S. Raman, and X. Yu. 2018. "Axial compression tests on seawater and sea sand concrete-filled double-skin stainless steel circular tubes." *Eng. Struct.* 176 (Dec): 426–438. https://doi.org/10.1016/j.engstruct.2018.09.040.

Liang, Q. Q. 2017. "Nonlinear analysis of circular double-skin concrete-filled steel tubular columns under axial compression." *Eng. Struct.* 131 (15): 639–650. https://doi.org/10.1016/j.engstruct.2016.10.019.

Liang, Q. Q. 2018. "Numerical simulation of high strength circular double-skin concrete-filled steel tubular slender columns." *Eng. Struct.* 168 (Aug): 205–217. https://doi.org/10.1016/j.engstruct.2018.04.062.

Liang, W., J. F. Dong, and Q. Y. Wang. 2019. "Mechanical behaviour of concrete-filled double-skin steel tube (CFDST) with stiffeners under axial and eccentric loading." *Thin Walled Struct.* 138 (May): 215–230. https://doi.org/10.1016/j.tws.2019.02.002.

Lu, H., L. H. Han, and X. L. Zhao. 2010a. "Fire performance of self-consolidating concrete filled double skin steel tubular columns: Experiments." *Fire Saf. J.* 45 (2): 106–115. https://doi.org/10.1016/j.firesaf.2009.12.001.

Lu, H., X. L. Zhao, and L. H. Han. 2010b. "Testing of self-consolidating concrete-filled double skin tubular stub columns exposed to fire." *J. Constr. Steel Res.* 66 (8–9): 1069–1080. https://doi.org/10.1016/j.jcsr.2010.03.004.

Lu, Q. R., L. H. Xu, Y. Chi, F. Q. Deng, M. Yu, and X. Hu. 2021. "A novel analysis-oriented theoretical model for steel tube confined ultra-high performance concrete." *Compos. Struct.* 264 (May): 113713. https://doi.org/10.1016/j.compstruct.2021.113713.

Mander, J. B., M. J. N. Priestley, and R. Park. 1988. "Theoretical stress strain model for confined concrete." *J. Struct. Eng.* 114 (8): 1804–1826. https://doi.org/10.1061/(ASCE)0733-9445(1988)114:8(1804).

Martin, D. O. S., and R. Q. Bridge. 1997. "Local buckling of thin-walled circular steel sections with or without internal restraint." *J. Constr. Steel Res.* 41 (2–3): 137–157. https://doi.org/10.1016/S0143-974X(97)80891-7.

Masaru, S., T. Fumihito, I. Toshiyuki, H. Atsushi, and K. Hirotaka. 2013. "Experimental study on ultimate strength of concrete filled double tubular steel with shear connector." *Int. J. Steel Struct.* 13 (1): 49–54. https://doi.org/10.1007/s13296-013-1005-x.

Mohammadbagheri, S., and B. Shekastehband. 2020. "Fire resistance of stiffened CFDST columns after earthquake-induced damages." *Thin Walled Struct.* 154 (Sep): 106865. https://doi.org/10.1016/j.tws.2020.106865.

MOHURD (Ministry of Housing and Urban-Rural Development of the People's Republic of China). 2010a. *Code for design of concrete structures*. GB/T 50010-2010. Beijing: MOHURD.

MOHURD (Ministry of Housing and Urban-Rural Development of the People's Republic of China). 2010b. *Metallic materials—Tensile testing—Part 1: Method of test at room temperature*. GB/T 228.1-2010. Beijing: MOHURD.

MOHURD (Ministry of Housing and Urban-Rural Development of the People's Republic of China). 2014. *Technical code for concrete filled steel tubular structures*. GB 50936-2014. Beijing: MOHURD.

Naeimi, N., and M. A. Moustafa. 2021. "Compressive behavior and stress-strain relationships of confined and unconfined UHPC." *Constr. Build. Mater.* 272 (Feb): 121844. https://doi.org/10.1016/j.conbuildmat.2020.121844.

Ozbakkaloglu, T., and Y. Idris. 2014. "Seismic behavior of FRP-high-strength concrete-steel double-skin tubular columns." *J. Struct. Eng.*

© ASCE

04021298-23

J. Struct. Eng.

140 (6): 04014019. https://doi.org/10.1061/(ASCE)ST.1943-541X .0000981.

Peng, K., T. Yu, M. N. S. Hadi, and L. Huang. 2018. "Compressive behavior of hybrid double-skin tubular columns with a rib-stiffened steel inner tube." *Compos. Struct.* 204 (Nov): 634–644. https://doi.org/10.1016/j .compstruct.2018.07.083.

Richard, P., and M. Cheyrezy. 1995. "Composition of reactive powder concretes." *Cem. Concr. Res.* 25 (7): 1501–1511. https://doi.org/10.1016 /0008-8846(95)00144-2.

Sakino, K., H. Nakahara, S. Morino, and A. Nishiyama. 2004. "Behavior of centrally loaded concrete-filled steel-tube short columns." *J. Struct. Eng.* 130 (2): 180–188. https://doi.org/10.1061/(ASCE)0733-9445 (2004)130:2(180).

Samani, A. K., and M. M. Attard. 2012. "A stress-strain model for uniaxial and confined concrete under compression." *Eng. Struct.* 41 (8): 335–349. https://doi.org/10.1016/j.engstruct.2012.03.027.

Shen, L., B. Yang, M. Ding, C. Feng, S. Alqawzai, M. Elchalakani, and K. Chen. 2022. "Experimental study on the behavior of a novel stiffened hexagonal CFDST stub column under axial load." *J. Struct. Eng.* 148 (1): 04021231. https://doi.org/10.1061/(ASCE)ST.1943-541X .0003198.

Tao, Z., and L. H. Han. 2006. "Behaviour of concrete-filled double skin rectangular steel tubular beam-columns." *J. Constr. Steel Res.* 62 (7): 631–646. https://doi.org/10.1016/j.jcsr.2005.11.008.

Tao, Z., B. Uy, F. Y. Liao, and L. H. Han. 2011. "Nonlinear analysis of concrete-filled square stainless steel stub columns under axial compression." *J. Constr. Steel Res.* 67 (11): 1719–1732. https://doi.org/10.1016 /j.jcsr.2011.04.012.

Tao, Z., X. Q. Wang, and B. Uy. 2013a. "Stress-strain curves of structural and reinforcing steels after exposure to elevated temperatures." *J. Mater. Civ. Eng.* 25 (9): 1306–1316. https://doi.org/10.1061/(ASCE)MT .1943-5533.0000676.

Tao, Z., Z. B. Wang, and Q. Yu. 2013b. "Finite element modelling of concrete-filled steel stub columns under axial compression." *J. Constr. Steel Res.* 89 (Oct): 121–131. https://doi.org/10.1016/j.jcsr.2013.07.001.

Teng, J. G., Z. H. Wang, T. Yu, Y. Zhao, and L. J. Li. 2018. "Double-tube concrete columns with a high-strength internal steel tube: Concept and behaviour under axial compression." *Adv. Struct. Eng.* 21 (10): 1585–1594. https://doi.org/10.1177/1369433217746838.

Uy, B., Z. Tao, and L. H. Han. 2011. "Behaviour of short and slender concrete-filled stainless steel tubular columns." *J. Constr. Steel Res.* 67 (3): 360–378. https://doi.org/10.1016/j.jcsr.2010.10.004.

Wang, W. Q., C. Q. Wu, J. Li, Z. X. Liu, and X. D. Zhi. 2019. "Lateral impact behavior of double-skin steel tubular (DST) members with ultra-high performance fiber-reinforced concrete (UHPFRC)." *Thin Walled Struct.* 144 (Nov): 106351. https://doi.org/10.1016/j.tws.2019.106351.

Wang, Z. B., J. B. Zhang, W. Li, and H. J. Wu. 2020. "Seismic performance of stiffened concrete-filled double skin steel tubes." *J. Constr. Steel Res.* 169 (Jun): 106020. https://doi.org/10.1016/j.jcsr.2020.106020.

Wei, S., S. T. Mau, C. Vipulanandan, and S. K. Mantrala. 1995. "Performance of new sandwich tube under axial loading—Experiment." *J. Struct. Eng.* 121 (12): 1806–1814. https://doi.org/10.1061/(ASCE) 0733-9445(1995)121:12(1806).

Wu, Z. M., C. J. Shi, W. He, and D. H. Wang. 2016. "Uniaxial compression behavior of ultra-high performance concrete with hybrid steel fiber." *J. Mater. Civ. Eng.* 28 (12): 06016017. https://doi.org/10.1061 /(ASCE)MT.1943-5533.0001684.

Xiong, D. X. 2012. "Structural behaviour of concrete filled steel tubes with high strength materials." Ph.D. thesis, Dept. of Civil and Environmental Engineering, National Univ. of Singapore.

Xiong, M. X., D. X. Xiong, and J. Y. R. Liew. 2017a. "Axial performance of short concrete filled steel tubes with high- and ultra-high-strength materials." *Eng. Struct.* 136 (Apr): 494–510. https://doi.org/10.1016/j .engstruct.2017.01.037.

Xiong, M. X., D. X. Xiong, and J. Y. R. Liew. 2017b. "Behaviour of steel tubular members infilled with ultra high strength concrete." *J. Constr. Steel Res.* 138 (Nov): 168–183. https://doi.org/10.1016/j.jcsr.2017 .07.001.

Yan, G. J. 2005. "Study on constitutive relationship and failure criterion of 200 MPa reactive powder concrete (RPC200)." Doctor of Engineering, School of Civil Engineering, Beijing Jiaotong Univ.

Yan, X. F., Y. G. Zhao, and S. Q. Lin. 2021. "Compressive behaviour of circular CFDST short columns with high- and ultrahigh-strength concrete." *Thin Walled Struct.* 164 (Jul): 107898. https://doi.org/10.1016/j .tws.2021.107898.

Yan, Y. X., L. H. Xu, B. Li, Y. Chi, M. Yu, K. K. Zhou, and Y. Song. 2019. "Axial behavior of ultra-high performance concrete (UHPC) filled stocky steel tubes with square sections." *J. Constr. Steel Res.* 158 (Jul): 417–428. https://doi.org/10.1016/j.jcsr.2019.03.018.

Yang, J., B. C. Chen, and J. Z. Su. 2020. "Effect of steel fiber on elastic modulus of ultra-high-performance concrete." [In Chinese.] *J. Chin. Ceram. Soc.* 48 (5): 654–658. https://doi.org/10.14062/j.issn.0454 -5648.20190604.

Zhang, F. R., C. Q. Wu, Z. X. Li, and X. L. Zhao. 2015. "Residual axial capacity of CFDST columns infilled with UHPFRC after close-range blast loading." *Thin Walled Struct.* 96 (Nov): 314–327. https://doi .org/10.1016/j.tws.2015.08.020.

Zhang, J. W., X. Y. Li, W. L. Cao, and C. Yu. 2019. "Cyclic behavior of steel tube-reinforced high-strength concrete composite columns with high-strength steel bars." *Eng. Struct.* 189 (Jun): 565–579. https://doi .org/10.1016/j.engstruct.2019.04.006.

Zhao, X. L., B. K. Han, and R. H. Grzebieta. 2002. "Plastic mechanism analysis of concrete-filled double-skin (SHS inner and SHS outer) stub columns." *Thin Walled Struct.* 40 (10): 815–833. https://doi.org/10 .1016/S0263-8231(02)00030-7.

Zhou, K., and L. H. Han. 2019. "Modelling the behaviour of concrete-encased concrete-filled steel tube (CFST) columns subjected to full-range fire." *Eng. Struct.* 183 (Mar): 265–280. https://doi.org/10.1016/j .engstruct.2018.12.100.

Zhou, Z., D. Gan, and X. H. Zhou. 2019. "improved composite effect of square concrete-filled steel tubes with diagonal binding ribs." *J. Struct. Eng.* 145 (10): 04019112. https://doi.org/10.1061/(ASCE)ST.1943 -541X.0002400.

Zhou, Z. D., and P. Z. Qiao. 2018. "Durability of ultra-high performance concrete in tension under cold weather conditions." *Cem. Concr. Compos.* 94 (Nov): 94–106. https://doi.org/10.1016/j.cemconcomp .2018.08.019.